KILOMETRIC RADIATION POWER FLUX DEPENDENCE ON AREA OF DISCRETE AURORA

by

N. A. Saflekos[1], J. L. Burch[2], D. A .Gurnett[3],

R. R. Anderson[3] and R. E. Sheehan[4]

1. University of Texas at San Antonio
Div. of Earth and Physical Sciences
College of Sciences and Engineering
San Antonio, TX 78285

2. Southwest Research Institute
Division 15
P. O. Drawer 28510
San Antonio, TX 78284

3. The University of Iowa
Department of Physics
and Astronomy
Iowa City, IA 52242

4. Boston College
Department of Physics
140 Commonwealth Avenue
Chestnut Hill, MA 02167

ABSTRACT

Kilometer wavelength radiation, measured from distant positions over the north pole and over the earth's equator, was compared to the area of discrete aurora imaged by several low-altitude spacecraft. Through correlative studies of auroral kilometric radiation (AKR) with about two thousand auroral images, a stereoscopic view of the average auroral acceleration region was obtained. A major result of this study is that the total AKR power increases as the area of the discrete auroral oval increases. The implications of this result are that the regions of parallel potentials or the auroral plasma cavities, in which AKR is generated, must possess the following attributes: (1) they are shallow in altitude and their radial position depends on wavelength, (2) they thread flux tubes of small cross section, (3) the generation mechanism in them reaches a saturation limit rapidly, and (4) their distribution over the discrete auroral oval is nearly uniform. The above statistical results are true for large samples collected over a long period of time (about six months). In the short term, AKR frequently exhibits temporal variations with scales as short as three minutes (the resolution of the averaged data used). These fluctuations are explainable by rapid quenchings as well as fast starts of the electron cyclotron maser mechanism. There were times when AKR was present at substantial power levels while optical emissions were below instrument thresholds. A recent theoretical result may account for this set of observations by predicting that suprathermal electrons, of energies as low as several hundred eV, can generate second harmonic AKR. Our indirect observations of second harmonic AKR require that these electrons have mirror points high above the atmosphere so as to minimize auroral light emissions. The results of this study provide evidence supporting the electron cyclotron maser mechanism.

INTRODUCTION

Magnetized planets and intermittent sources near magnetized stars all have a common property in that they give off powerful electromagnetic emissions in the radio frequency range. It is believed that all these emissions owe their generation to the same production mechanism (see the review by Dulk [1985]). For the earth in particular, extensive observations have been accumulated since the discovery of radio emissions by Benediktov et al. [1965]. The terrestrial radio emissions with wavelengths close to one kilometer have been associated with nightside aurora and are called auroral kilometric radiation (see the reviews by Gurnett [1983] and Benson [1985]).

Auroral kilometric radiation (AKR) is a radio emission in the frequency range 50 to 700 kHz. This radiation is the most intense auroral plasma emission with a spectrum that peaks near the 250 kHz frequencies. Within the auroral oval the magnetic local hour sector with the strongest radio source is the one at 2200 MLT. Global observations of AKR show rapid temporal variations characterized by intense impulsive bursts which are usually associated with discrete aurora (Gurnett, 1974). Other high latitude phenomena indirectly related to AKR are: auroral electrojets (Voots et al., 1977); field-aligned currents (Green et al., 1982); and electron inverted V's (Green et al., 1979).

Several mechanisms have been proposed for the generation of AKR and most of them involve the electron cyclotron maser instability first reported by Wu and Lee (1979). A search for sources of energy that could produce AKR was conducted by Dusenbery and Lyons (1982) and they found two distributions of electrons suitable for that purpose. The first was

accelerated precipitating electrons with energies between 1 to 10 keV, and the second was electrostatistically trapped upgoing electrons with deep loss cones. Winglee (1985a,b) has shown that the electron cyclotron maser instability can generate AKR in the X, O, or Z mode and that the dominant radiation is in the mode with the largest growth rate when the maser instability saturates. The dominant mode depends not only on the ratio of the ambient plasma frequency ω_{pe} to the electron gyrofrequency Ω_e but on the form of the electron distribution function as well. Remote observations of AKR helped establish the location of the source region (at 1.5 to 3 R_E altitude and ~ 70° magnetic latitude above the nightside auroral zone as reported in the works of [Gurnett, 1974; Kaiser and Alexander, 1977; Kaiser et al., 1978; Gurnett and Green, 1978; Gurnett et al., 1983; Gurnett and Shaw, 1973]. The physical conditions in or near the AKR sources have been most dependably determined by the ISIS 1 satellite [Benson and Calvert, 1979; James, 1980]. This knowledge narrowed down the field of the emission processes and gave a good sense of direction to theoretical investigations.

It is universally accepted today that AKR is mainly emitted in the first harmonic of the right handed X-mode cutoff frequency

$$\omega_x \simeq \Omega_e (1 + \omega^2_{pe}/\Omega_e^2) \quad \text{for} \quad \omega^2_{pe}/\Omega_e^2 << 1$$

Correlative studies between AKR and other auroral phenomena have established that discrete auroral arcs are associated with bursts of AKR which occur during electron inverted-V events endowed with energies 5 to 10 keV (refer to the works of Green et al., 1979; Benson et al.,

1980; Green et al., 1982; Kaiser et al., 1978; Shawhan and Gurnett, 1982). Some experimental facts of theoretical importance are:

(a) The strongest X mode events take place inside regions depleted of background electrons ($\omega_{pe}/\Omega_e << 0.4$ for weak events and $\omega_{pe}/\Omega_e << 0.2$ for the strong events) [Benson and Calvert, 1979; Calvert, 1981a; Benson, 1985].

(b) The AKR frequency bandwidth is very narrow ($\delta\ \omega/\omega \leq 0.01$) [Gurnett et al., 1979].

(c) The distributions of energetic electrons above AKR source regions are nonthermal [Mizera and Fennel, 1977], most likely due to downward electrostatic acceleration and upward magnetic mirror forces.

(d) The distributions of energetic electrons above AKR source regions also have deep loss cones due to ionospheric absorption of small pitch angle electrons [Chiu and Schulz, 1978].

In the last ten years one mechanism that makes use of the above facts has emerged as the best candidate for explaining the AKR properties. It is a relativistic Doppler-shifted electron cyclotron resonance process first proposed by Wu and Lee [1979] as mentioned above.

Many subsequent papers were devoted to the calculation of linear growth rates of AKR modes [Lee and Wu, 1980; Lee et al., 1980; Wu et al., 1981a, b, 1982; Dusenbery and Lyons, 1982; Hewitt et al., 1982; Melrose et al., 1982; Omidi and Gurnett, 1982; Wong et al., 1982;

Freund et al., 1983; Hewitt and Melrose, 1983; Wagner et al., 1983, 1984; Le Quéau et al., 1984a, b; Omidi et al., 1986; Prichett, 1984a, b; Strangeway, 1985; Pritchett and Strangeway, 1985]. All the above authors have used either measured or modeled electron distribution functions to predict the maximum growth rates. Furthermore, in all the above works it was tacitly assumed that the plasma is homogeneous everywhere in the source region. However, near the cutoff frequency toward lower altitudes the refraction should depend both on transverse gradients of background plasma densities and on parallel gradients of the real magnetic field. Thus factors that influence the refraction should also influence the amplification of the plasma wave emission. Omidi and Gurnett (1984) have used inhomogeneous magnetic field and homogeneous plasma in the source region to determine the integrated gain. Le Quéau et al. (1985) have shown that the homogeneous resonance condition is only satisfied over an altitude range less than the wavelength (~ 1 km) with propagation vector parallel to the magnetic field. In fact they estimated the source size for one frequency to be about 20 km in altitude and about 100 km in longitude. Furthermore, Zarka et al. (1986) have shown that no X-mode generation can occur if ω_{pe}/Ω_e is too large in the source region.

As with all resonance mechanisms the saturation is thought to be due to the affect of the generated mode back upon the population of particles providing the free energy for the growth of the waves during the time that the plasma becomes unstable. Zarka et al. (1986) have computed the spectral intensity at a distance R from the source as a function of the parallel kinetic energy. For a frequency of 250 kHz and a distance of 7 R_E the logarithm of the spectral density varies linearly with parallel energy. Two points on the theoretically computed curve are (1×10^{-22} W-m^{-2} - Hz^{-1}, 10 keV) and (1×10^{-13} W-m^{-2} - Hz^{-1}, 20 keV). They are to be

compared to corresponding observations at 250 kHz AKR intensities, normalized to 7 R_E, of 10^{-19} and 10^{-13} W-m^{-2} - Hz^{-1} at 1 and 10 keV electrons respectively, in the strongest inverted V events [Gurnett, 1974; Kaiser and Alexander, 1977]. The brightness temperature of an AKR source is defined as $T_B = I_v \lambda^2/2\text{-}k\Omega$ where I_v is the intensity [W-m^{-2} - Hz^{-1}, λ is the wavelength [m], k is the Boltzmann constant [joules/^oK], and Ω_e is the solid angle subtended by the source [rad^2]. For an intensity of 10^{-19}W-m^{-2} -Hz^{-1}, a wavelength 1.2 x 10^3 m, and a solid angle of 2.2 x 10^{-3} rad^2, the brightness temperature corresponds to 1 x 10^{18} ^oK. Similarly for the same wavelength and solid angle the intensity of 10^{-13} W-m^{-2} - Hz^{-1} corresponds to a brightness temperature of 10^{25} ^oK. Such brightness temperatures are possible only if nonthermal electrons from 10 to 20 keV are present in the source region. These energies are greater by factors of 2 to 10 than the ones present in strong inverted V events. One way out of this predicament is a laser process where the partial reflection of AKR at steep density gradients on the boundaries of the source region causes further amplification of the wave as proposed by Calvert (1982).

In this paper we will find applicable the main ideas incorporated in a fully inhomogeneous theory of electron cyclotron maser instability of Le Qéau et al. (1985) and of Zarka et al. (1986). They are: (a) The spatial limitation of the source region for any one AKR frequency is ~ 20 km in altitude range and ~ 100 km in any direction transverse to the ambient magnetic field. (b) The quenching of usual saturation mechanisms by inhomogeneity such as the vertical magnetic field gradient and the background plasma density in the source

region. (c) AKR R-X mode waves are generated directly through the electron cyclotron maser instability by the weakly relativistic electrons (1 - 10 keV) usually found over discrete aurora.

We will test the hypothesis that the distribution of AKR sources is proportional to the area of the discrete aurora and that the brighter AKR sources are associated with brighter discrete auroras believed to be produced by more energetic electrons in the range 1 to 10 keV. This last hypothesis is made plausible by the limited altitude extent of the AKR source, the saturation of the maser instability and the production of AKR by electron energies found over discrete auroras. Furthermore, the pitch angle distributions of electrons over discrete auroras are compatible with AKR production mechanisms. Some reasons why background electrons usually have $\omega_{pe}/\Omega_e < .4$ are: the presence of parallel electric fields, the mirror force, and the atmosphere. We adopt the observational results that the most frequent mode of AKR emissions is in the right-hand X mode (first harmonic) in plasma cavities with $\omega_{pe}/\Omega_e < 0.4$ for the medium AKR events or and 0.2 for the strong AKR events already mentioned above.

OBSERVATIONS

A. Simultaneous Isis 2 and Hawkeye Observations

The following data analysis for ISIS-2 was completed by Murphree and Anger (1980). Here we repeat their main ideas for completeness. The global distribution of aurora has been determined by an auroral scanning device on ISIS-2 satellite. Based upon Auroral Scanning Photometer data from ISIS-2, Murphree and Anger found that the instantaneous auroral distribution is continuous from the afternoon sector through midnight and into the morning. Cogger et al., (1977) and Buchau et al., (1970) have shown that the continuity of optical emissions in the noon sector depends upon the wavelength sampled. In addition to the question of morphology of aurora there is the problem of determining the actual intensity distribution on an instantaneous basis and the interpretation of such measurements at different local times in relation to magnetospheric activity. The Auroral Scanning Photometer (ASP) on ISIS-2 (see Anger et al., 1973 for details) is well suited to answer this question as it monitors two of the prominent auroral emissions, 5577 and 3914 Å. This quantitative information is especially significant because it allows the ratio I(5577Å)/I(3914Å) to be determined, which can then be used to infer characteristic energies of the precipitating particles emanating from different regions of the plasmasheet. The auroral distribution over almost the entire northern hemisphere was observed by the ASP within a time period of less than 15 min. Data for this one pass were taken from 0612 to 0627 UT on December 16, 1974. The pass occurs at the leading edge of a small broad peak in AE (maximum value 250 nT) and thus may represent the early stage of a substorm. The position of the equatorward boundary of the aurora at 24 MLT was 66° invariant latitude.

Figure 1 top picture shows the 3914Å data transformed into a corrected geomagnetic latitude and time grid. The coordinate grid is superposed on the image. The 5577Å measurements are similar. The observations have been corrected for pathlength absorption (Van Rhijn effect) but not for surface albedo effects. Because of the limitation in the dynamic range of the picture, low intensity regions are visible while higher intensity regions tend to be smeared out. Discrete aurorae can be recognized as spatially confined intense regions of intense light distribution while diffuse aurorae are relatively uniform emissions of lower intensity.

In order to define more quantitatively the limits of optical emission, Murphree and Anger (1980) has calculated poleward and equatorward boundaries of emission shown in Figure 1, lower left polar plot. These boundaries are derived from intensity profiles taken one hour apart in magnetic local time (MLT) and corrected for surface albedo as well. The boundaries are taken at the transition points between the background emissions (airglow plus noise) and auroral features. They are calculated by taking separate cumulative averages of the poleward and equatorward 5577 and 3914 Å intensities while moving toward the auroral oval. The boundary is defined to be that latitude at which the intensity exceeds 2.5 times the value of the standard deviation in the average background intensity. No boundaries are shown for the 11 or 12 MLT due to a gap in the emissions there. Using the above calculated boundary positions, Murphree and Anger have obtained the average 5577 and 3914 Å intensities for each MLT. The results are sown in the bottom right cartesian panel of Figure 1 along with the peak 3914Å intensity. As expected, there are significant changes of intensity with MLT. From noon the intensities gradually increase toward an enhancement region at 14-15 MLT (peak intensity of 3914Å of 2.5 kR) after which the intensity for both wavelengths decreases. A discrete arc is

encountered starting at approximately 18 MLT, and the highest average intensities are encountered in this system at 22 MLT (5.6 kR for 5577Å). A gradual decrease in intensity is seen toward the morning until the gap at 10 MLT. Aside from the regions of peak intensity between 20 and 02 MLT, average intensities are on the order of 1 to 2 kR and represent mainly diffuse auroral emissions.

Murphree and Auger (1980) further describes the data as follows. Individual intensity measurements for each MLT have been used to determine the average ratio I(5577 Å)/I(3914 Å). In order to eliminate the problem of biased ratio (see Eather and Mende, 1972) an average ratio for each MLT has been calculated by taking the logarithm of each individual ratio, averaging, and then taking the anti-logarithm. The result for each MLT is shown at the upper cartesian panel on the lower right hand side of Figure 1. The errors shown represent the standard error in the average ratio determined at each MLT. One of the complications of this analysis is that for any point along the profile the 5577 and 3914Å intensities are determined with a delay setting them 9.36 seconds apart. Even small variations in intensity over this time scale will result in significant variations in the ratio, although the average value should not be affected. Variations in the ratio from point to point along a profile become especially important on the dayside where there is more uncertainly in the background emissions and where the extent of the auroral distribution is less. This is reflected in the relatively large variations in this region (see 09 MLT, for example). The variation in ratio as a function of MLT implies considerable variation in the energy of the precipitating particles around the auroral distribution. Rees and Luckey (1974) have shown that it is possible to calculate the characteristic energy of the precipitating particles by using certain auroral spectroscopic ratios. The ratio I(5577Å)/I(3914Å) while not optimum for this type of analysis (Mende and Eather,

1975; Eather, 1979) can, nevertheless, be used to infer a characteristic energy. There are at least four drawbacks in this technique:

a) Lack of knowledge on proton precipitation;

b) Necessity to assume a shape for the primary particle energy spectrum;

c) Lack of knowledge of primary particle pitch angle distribution;

d) Variation in the ratio with 3914Å intensity.

It is nevertheless useful to estimate characteristic energies from the observed ratios in various time sectors. These are obtained by imposing the following conditions:

a) Only electron precipitation is considered;

b) The primary spectrum is taken to be Maxwellian in form;

c) An isotropic pitch angle distribution is assumed;

d) No variation in ratio with 3914Å intensity is considered.

Using the average ratios calculated for each magnetic local time, Murphree and Anger (1980) have calculated the characteristic energies. The resulting estimates varied from 0.5 - 0.8 keV (late afternoon) to 2.5 - 3.5 keV (morning).

In addition to causing the aurora (Hoffman et al., 1985), these higher energy electrons from premidnight to morning cause the Auroral Kilometric Radiation (Holzworth et al., 1977; Lee et al., 1980). During this time required to form the global image of the auroral oval with the ISIS-2 satellite a second satellite, the Hawkeye, measured the AKR power flux emitted by the aurora. The power flux varied from (5.5 to 9) x 10^{-18} ($W\text{-}m^{-2}\text{-}Hz^{-1}$) (see Figure 2) characteristic of moderate auroral activity. It is most probable that a large amount of AKR came from the 2200 MLT hour sector with peak values exceeding 10 kR.

B. Simultaneous ISEE-1 and DMSP Observations

This section considers in some detail the relationship between aurorae seen in DMSP satellite images and ISEE-1 AKR observations between 10 and 22 R_E relatively close to the equatorial plane (< 35° solar magnetic, SM, latitude). The first part presents two examples of closely timed auroral images ($\lesssim$ 10 minutes) during AKR enhancements. Events like this are vital to demonstrate the actual connection between aurorae and AKR, both of which can vary tremendously in a matter of minutes. The second part involves the location of ISEE-1 measurements at four frequencies and three levels of AKR intensity with simultaneous auroral activity.

1. Simultaneous AKR and Auroral Observations

In this section of the paper we present several examples of DMSP auroral images and AKR activity. Figure 3 (from Gallagher and Gurnett, 1979) illustrates the geometry of AKR ray propagation originating in each separate hemisphere. It depicts a time averaged situation with AKR sources over the auroral zones in a noon-midnight meridional plane. Green et al. (1979) found frequency dependent emission cones illuminating most of the nightside magnetosphere and a large portion of the dayside magnetosphere. The plasmaspheric cutoff surface produces a shadow zone centered about the equatorial plane. From the heights where sources are believed to occur (~ 1 - 3 R_E), AKR generally should not be seen within 12 R_E near equatorial solar magnetic latitudes. With the discovery of higher harmonic AKR this idealized picture will not represent the real situation at all times. Although the most intense sources appear to be located in the 2200 to 2400 MLT sector, sources at other local times have also been observed.

Figure 4 displays part of an ISEE survey plot from 1200 to 2000 UT on January 22, 1979 in the upper panel. The bottom panel is a plot of the ISEE orbit beginning at 0400 UT on January 22, and ending at 2400 UT January 23, 1979. Electric field intensities from 0 to 100 dB are stacked from top to bottom for the 300, 178, 100, and 50 kH_z channels. Average and maximum intensities in 140 second long intervals are indicated by the solid area and the line above it, respectively. Vertical lines in the electric field plot indicate DMSP images discussed in subsequent figures. ISEE-1 positions corresponding to the images at 1258 UT, near 1430 UT, and near 1800 UT are marked by arrows in the orbit plot. The solar magnetic Z axis points northward along the magnetic dipole axis, the Y points approximately toward dusk,

and represents the distance from the Z axis projected onto the equatorial plane. The longitude range for this orbit is only about 30° which is small enough to allow consideration of this plot almost in the dawn-dusk plane.

Figure 5 top drawing is a sketch of the DMSP image (orbit number 3781) taken near 1258 UT on January 22, 1979. Corrected geomagnetic latitude (CGLT) circles at 60° and 70° are shown along with the 1900 and 2300 corrected geomagnetic local time (CGLT) meridians. A discrete arc indicated by solid black area extends along the 70° CGLT from about 1800 to 2300 CGLT. The large stippled area denotes diffuse aurora appearing at lower latitudes. From 2100 to 2300 GGLT the discrete arc is broken in appearance, like the remnant of an auroral bulge formed after substorm onset. In fact, the AE index (bottom of Figure 5) peaked at 500 nT about 20 minutes before the image time and decreased to about 300 nT at the image time. Just after this image the AE index again increased to 600 nT at 1315 UT. The arrow in the orbit plot (bottom of Figure 4) indicates that ISEE was located near 16 R_E at about 25° SMLAT. The AKR intensities (Figure 4 top) seem to be particularly intense (~ 10^{-13} W-m^{-2} - Hz^{-1} at 300 and 178 kHz) especially in light of the relatively small area of discrete aurora in the image. Figure 5 (top) is an example of an isolated DMSP image, a "snapshot" of the aurora, which in the past has been the only type of direct comparison between aurorae and AKR (Gurnett, 1974; and Saflekos et al., 1983).

In Figure 6, two DMSP images taken about 10 minutes apart near 1430 UT show discrete aurora before midnight about 70° CGLAT and diffuse aurora below 70° CGLAT. At this time ISEE was located at approximately 17 R_E and 20° SMLAT. AKR intensities (Figure

4) were decreasing from peaks attained near 1300 UT. Considering the AE index alone, which fell below 100 nT after 1420 UT, one would not expect strong auroral activity, but the DMSP images suggest that a slight disturbance occurred sometime after 1425 UT. The discrete aurora in image 3782 moved poleward and westward from its position about 10 minutes earlier in image 12236, and had a looplike appearance suggesting a small westward traveling surge. AKR activity also showed slight but definite increases during this time period, particularly in the 300 and 178 kHz channels (see Figure 4).

A slightly larger auroral intensification appears in Figure 7. This time three DMSP images trace the auroral development from a broad diffuse band at 1750 UT (upper left) to discrete arcs at 1754 UT (upper right) and at 1801 UT (bottom of Figure 7). The AE index (Figure 5) started below 50 nT at 1740 UT, increased slowly to 100 nT at 1800 UT, and then grew steadily to over 1000 nT at 2030 UT. ISEE (Figure 4) moved out to 19 R_E and approached the equatorial plane to within 8° SMLAT. AKR intensities rose gradually with the AE index at 1740 UT, but sharp increases at all frequencies before 1800 UT appear to reflect the enhanced auroral activity seen in the images. Again, the AKR burst was largest at the higher frequencies, although in this case a strong jump at 100 kHz was superposed on a weak background.

2. Statistical Results

AKR data for this study were taken from survey plots of the electric spectrum analyzer aboard the ISEE-1 satellite. The four highest frequencies at 50, 100, 178, and 300 kHz span a substantial portion of the typical AKR spectrum which speaks at around 250 kHz. ISEE travels in an elliptical orbit with perigee and apogee at about 1.4 and 22.3 R_E,

respectively. The data included in this study were taken during January 1979 when the far nightside part of the orbit lay in the 0400 - 0600 MLT sector. At this time three active DMSP satellites provided an unusually large number of auroral images. Favorable lighting conditions over the north pole allowed a large portion of these to be of good quality, except at full moon. Similar conditions prevail over the southern hemisphere from May to August, but since ISEE remains in the northern tail lobe most of the time, any comparison between AKR and aurora would depend implicitly on magnetic conjugacy of the aurora.

Sheehan et al. (1982), found that a simple rating scheme for DMSP images can reliably characterize auroral activity as do K_p and AE. The criteria for auroral activity (brightness and extent) are roughly analogous to the characteristics of precipitating electrons believed to govern AKR intensity. DMSP radiometers have broad passbands extending from long visible through near infrared wavelengths. The response usually has a small dynamic range thus all but the weakest auroras appear saturated in an image. Brightness criteria apply best when distinguishing between quiet and moderate auroral conditions; auroral extent is the best way to discriminate between moderate and active conditions. The general criterion for the active category is bright aurora extending 5° or more in latitude over several hours of local time. Images at this level often, but not always, resemble the classical substorm expansion and break-up phases.

Figures 8a through 8d are a group of scatter plots of AKR measurements from ISEE and observations of auroral images from DSMP during the month of January, 1979. Figure 8a is for conditions of active aurora. Each dot represents the location of ISEE at the time of an active aurora was imaged. The top row of panels depicts the 300 kHz channel, the

bottom row the 178 kHz channel. From left to right the panels represent cases with powers (P_7 normalized to point sources at the center of the earth and observed from 7 R_E away)

$$P_7 \geq 10^{-14},\ 10^{-15} \geq P_7 \geq 10^{-17},\ \text{and}\ P_7 \leq 10^{-18} W - m^{-2} - Hz^{-1}$$

corresponding to intense, intermediate, and weak respectively. This crude correction is sufficient given the order of magnitude of intensity steps used here. Spectral fluxes were determined from calibration tables and scalings of the survey plots, so that only order of magnitude precision is justified in any case.

ISEE observations are plotted in bins1 R_E radial distance by 2° SM latitude. All ISEE measurements in Figures 8a through 8d are for SM longitudes between 240° and 270° or 0400 - 0600 MLT. Both the 300 and the 178 kHz frequency channels show similar behavior. The most intense cases tend to occur at SM latitudes greater than 10°. Intermediate AKR intensities are distributed nearly uniformly from 0° to 20° SM latitude and outside 15 R_E (the inward limit of ISEE observations on the SM equatorial plane). Instances of weak AKR intensity occur most often within 10° of the SM equator. Figure 8b shows ISEE positions at times when DMSP was imaging moderate auroral activity. Here again both the 300 and 178 kH_z channels, show intense power occuring at SM latitudes greater than 10°. Intermediate AKR intensities are distributed nearly uniformly from 8 to 20° SM latitude and outside 15 R_E radial distance. Instances of weak AKR intensity occur most often within 10° of the SM equator. In Figure 8c active auroral image category and AKR observations in the frequency

channels 100 and 50 kH_z are plotted in the format of Figure 8a. The shift in the position of the points with decreasing AKR intensity is somewhat different than that in Figure 8a. There are fewer cases in the more intense category but they too occur most often at high SM latitudes. More cases have shifted from intense to intermediate AKR levels, and the latitude distributions in the weak AKR category are broader than those seen for weak AKR in Figure 8b.

The subtotal number of points for each category in Figure 8a through 8d are shown in Figure 9 as number of cases for each decade of power from 10^{-18} to 10^{-14} $W \cdot m^{-2} \cdot Hz^{-1}$, separated by frequency channel. The middle three AKR power decades represent the average power of intermediate AKR intensity. Active auroral conditions are indicated by Δ's and moderate with filled circles. Clearly the number of moderate-aurora images for all frequencies in the weak AKR intensity category exceeds the number of active-aurora images. The reverse is true of the intermediate and the intense AKR categories. By far the most frequent occurrence belongs to the lowest power decade. In the intense AKR category the frequency of occurrence decreases with decreasing frequency.

It is interesting to point out here that of all the observations in the intense AKR category, inside the southern hemisphere, there are none corresponding to the 100 and 300 kHz channels, one to the 178 kHz channel, and five to the 50 kHz channel. Counted in the above cases were both moderate- and active-aurora images. A significant result is that at the highest power level there are more cases during active aurora than during moderate aurora. This argues in favor of an even distribution of AKR sources in a discrete-aurora area.

It also implies that as the auroral area, illuminated by energetic electrons, increases so does the total AKR power emitted by the collective distribution of AKR sources.

C. Simultaneous Hawkeye AKR Observations with All-sky Camera Pictures and DMSP Images

In this section we will first compare on a case by case basis the AKR power from Hawkeye at distant polar regions with all-sky camera pictures and second the AKR power with DSMP discrete aurora images. Finally we will compare statistically the 178 kHz AKR intensity from Hawkeye at high polar altitudes with discrete auroral images from DSMP at low altitudes.

1. Simultaneous Hawkeye AKR Observations with All-sky Camera Pictures

In the past cross correlations between AKR global measurements and local auroral phenomena showed a considerable amount of scatter rather than clear functional relations. To illustrate this point we show in Figure 10 observations of three minute averages of AKR power flux from Hawkeye and snapshots of aurora taken one minute apart by an all-sky camera belonging to the Air Force Geophysics Laboratory (AFGL). The logarithm of the 178 kHz AKR power flux is plotted as solid dots in the panels above the pictures. The AKR radiation was normalized to a distance 7 R_E away from the earth. The dark bands with pictures of the aurora represent filmed events as observed from the U.S. Air Force jet flying in the midnight local time sector (courtesy of Charles P. Pike). From 0900 to 0930 UT the AKR power flux remained below about 10^{-17} W - m^{-2} - Hz^{-1}. In the corresponding time interval the overhead aurora was practically missing, indicating AKR sources were present at locations different from

those visible with the all-sky camera (ASC). From 0930 to 0940 UT the auroral activity increased continuously reaching a level of 10^{-16} W - m^{-2} - Hz^{-1} at about 0937 UT. The ramp increase of AKR coincides with the spreading of the luminous area in the all-sky camera field of view. In direct contrast to the above, however, in the interval 0945 to 1001 UT the AKR power flux anticorrelates with the brightness of the all-sky camera picture in spite of the fact that the local aurora is brightest during this 16 minute interval in comparison to the entire 2 hour monitored period. Thus the nature of the distribution of electrons in energy and pitch angle must play a role different than that of high energy precipitating fluxes, presumably responsible for bright auroral emissions. Since the area of luminous auroral regions is so dynamic in nature due to the temporal variations of local auroral electron distributions it is not surprising that global observations of AKR would disagree with the presence of locally observed optical emissions. From 1004 to 1026 UT AKR power flux was bracketed by the levels of 10^{-16} to 10^{-15} W - m^{-2} - Hz^{-1}. The corresponding all-sky camera pictures showed auroral arcs either directly above the camera or near the horizon. Finally, in the last time interval from 1030 to 1100 UT the AKR power flux stayed below the 10^{-17} W - m^{-2} - Hz^{-1} and the observed aurora consisted of a faint arc near the horizon. These simultaneous high time resolution observations suggest that magnetic conjunction observations need to be made inside the source region and its concomitant auroral form below in the ionosphere if better correlations are to be found.

2. Simultaneous Hawkeye AKR Observations and DMSP Images

Some examples of the relationship between AKR power and auroral activity will be shown in the next series of figures. Three images from the DMSP satellites were

selected on the basis of auroral forms and magnetic activity. The images were taken during the time interval December 6-10, 1974. Each of the following figures (Figures 11 to 13) is a north hemisphere DMSP image gridded with corrected geomagnetic (CG) latitude circles and corrected geomagnetic local time meridians. The DMSP satellite track (not shown) projects down to the image central axis. Imaging scans are made transverse to the satellite velocity as the satellite moves equatorward in the night sector. The universal time axis indicating the evolution of the image construction is shown at the left of the figure. Horizontal bars extending to the right of the time axis indicate that AKR power flux density of the 178 kHz channel. The three minute averaged power was adjusted for observations at 7 R_E and corrected for r^{-2} dependence.

The AKR power points are centered at the midpoint of the three minute averaging interval. In order to compare the time of the imaging to the substorm phase an inset of the AE index versus time was included in Figures 11 through 13. A vertical line in the AE inset marks the approximate time of the image formation. Figure 11 shows orbit 3816 of the DMSP satellite 7529 on December 10, 1974. The image shows faint auroral arcs near the 70° and 75° CGM latitudes. Around 2300 CGLAT a westward traveling surge is in process with a bulge at around 73° CGLAT. This auroral event was accompanied by weak AKR power flux density 10^{-18} W - m^{-2} Hz^{-1} and low AE ($\simeq$ 250 nT). Even though the discrete aurora has the appearance of intense local arcs with some signs of broader disturbance features near 2300 CGM local time, the area illuminated is very small and the activity is classified as quiet. That is consistent with the weak AKR observed. Figure 12 is similar to Figure 11 except for orbit 6784 of a DMSP satellite. The image was taken around 1500 UT on December 8, 1974 and

shows a more active auroral form in comparison to that of Figure 11. On the equatorward side there are wide patches of diffuse aurora especially post-midnight. Poleward of 67° CGLAT there are multiple auroral arcs. The illuminated area in this image is about an order of magnitude greater than that of Figure 11. The AKR power emitted during the present event is also about an order of magnitude greater than the preceding event. Here we assume that the diffuse aurora is not associated in any way with the AKR source distribution. The area is considered moderate and the power intermediate. Thus we see that the bigger the discrete auroral area is the greater the AKR power (though the relationship is not a linear one). Figure 13 is an image taken during an intense substorm (AE $\simeq$ 500 nT). On December 9, 1974 the DMSP satellite 7529 traversed the nighttime auroral oval in the southward direction. During orbit 6795 it encountered a broad auroral form covering a zone of about 10 degrees in latitude and more than 60 degrees in longitude. It is possible this activity extends beyond the east and west limits of the image. The AKR power measured during this image's formation period was 10^{-14} W - m^{-2} - Hz^{-1}. Obviously, the power is about three orders of magnitude greater than that of the previous two images. The area is considered active and the power intense. The power cannot be accounted for by increase of area arguments alone. Saturation of the cyclotron maser instability and dense distribution of the AKR sources has to be invoked. It is not possible to discern detailed structure in this image because the DMSP radiometers are easily saturated by such intense auroral emissions. The AKR power observed is near the all time high (10^{-13} W - m^{-2} - Hz^{-1}).

3. Statistical Results

A large sample of DMSP auroral images (1178 total) is compared to AKR power flux from the Hawkeye satellite. Hawkeye had an inclination of 89°, apogee of 22 R_E, and orbital period of 52 hours. It was able to monitor AKR for about 46 hours per orbit. Measurements taken with the plasma and radio wave instrument on Hawkeye were averaged over three minutes and the point closest in time to the imaging of the centroid of the nightside aurora was kept for each image. Each measurement was adjusted for inverse square distance variation and was normalized to observations at 7 R_E geocentric distance. The logarithm of the AKR power flux density in the 178 kHz channel is used to correlate with the area of the discrete aurora.

The images were classified in six categories of auroral activity mainly on the basis of luminous area due to discrete aurora. The six levels of activity were characterized from low to high as: none observed (N), quiet (Q), moderate (three levels: M^-, M, M^+), and active (A). Figure 14 was constructed using only 572 data points of AKR power and auroral activity. The power range is from 10^{-18} to 10^{-13} W - M^{-2} - Hz^{-1}. The DMSP auroral activity comprises six discrete levels N to A. Column M has the maximum number of points (146). To the extreme left of M column N has the minimum number of points (28), and to the extreme right of N column A has a moderate number of points (113). It appears that the categories can easily be reduced to three by combining neighbors two at a time without changing any of our conclusions. Columns (N+Q) will make up the category Small Area, (M^-+M) the Medium Area, and (M^++A) the Large Area; Small, medium, and large for short will refer to the area of the

discrete aurora. Before we pass to this coarse analysis we would like to point out that the maximum AKR power in each of the (N to A) categories increases as one goes from N to A (see Figure 15). In this semilogarithmic plot there is a suggested linear relationship between the logarithm of the maximum AKR power and the coarse area of the discrete aurora.

Zarka et al. (1986) have computed the spectral intensity at 25 R_E, and the maximum electric field amplitude in the AKR source region as a function of the parallel kinetic energy in the AKR source region (see their Figure 6). Our Figure 15 showing the strongest events in each coarse level of auroral activity is very similar to Figure 6 of Zarka et al. (1986). This similarity may imply that during times of stronger auroral activity there are more electrons with greater parallel electron velocities reaching the AKR source region. The maximum power flux for 178 kHz AKR that was observed here after normalization to 7 R_E was 10^{-13} W - m^{-2} - Hz^{-1}. This value probably represents the limit set by the saturation level of the electron cyclotron maser instability. Except for the strongest events, during which the saturation seems to be reached in the source region, the generation of AKR appears to be a quasi-linear process. Calvert (1981b) has proposed a feedback mechanism whereby the radiation partially reflects at the boundaries of the source region and leads to larger amplification of the generated AKR power flux density. In a way this trapping and amplifying mechanism is laserlike.

Figure 16 is the distribution of 1178 images and corresponding simultaneous AKR power flux points in three different categories of discrete auroral area. The top panel corresponds to the small area category. Clearly the highest number of images with small area

of discrete aurora were associated with very weak AKR power (10^{-19} to 10^{-18} W - m^{-2} - Hz^{-1}). On the other hand there were no cases of small-area discrete auroral images with power in the highest decade (10^{-14} to 10^{-13} W - m^{-2} - Hz^{-1}). The medium-area category is characterized by a distribution of power flux which is bimodal. Nearly half or about 500 images appear below 5 x 10^{-17} W - m^{-2} - Hz^{-1} power flux and half above. The bottom panel considers discrete-aurora images with large areas. Clearly the highest number of these images falls in the power range 10^{-16} to 10^{-14} W - m^{-2} - Hz^{-1}. Here the highest decade of power is populated by a relatively large number of images in comparison to the same decade in the middle and top panels. The middle panel tends to behave half the time like an AKR source of small-area aurora and half the time as an AKR source of large-area aurora. Thus it isn't only the area of discrete aurora that is important in the global generation of AKR but the types of electron pitch angle- and energy-distributions also matter. Apparently the number of individual sources and the level of saturation of the maser instability in each source, on the average, increase as the discrete auroral area increases. It is well known that, under very active aurora, field-aligned currents intensify and inverted-V electron distributions. Thus field-aligned electrons and hardened electron spectra provide the source of energy for AKR power generation. Furthermore, the results of this study are consistent with the saturation property of the electron cyclotron maser instability.

DISCUSSION

The upper atmosphere constitutes a global fluorescent screen which is bombarded by energetic electrons originating in various magnetospheric plasma regions and producing visible light emissions known as aurorae. There are two types of aurorae in each hemisphere: (1) diffuse aurora characterized by its uniform weak glow and extending over large distances in zones surrounding the north and south geomagnetic poles, and (2) discrete aurora characterized by its intense brightness and spatio-temporal variations. The two types of aurorae are produced by different distributions of precipitating charged particles accelerated by a variety of mechanisms.

The discrete-aurora main acceleration region is found at radial distances typically between two to four earth radii. Spacecraft like the DE-1 and DE-2 probing this region from above and from below have measured ion and electron distributions whose characteristics are consistent with the presence of parallel electric fields. Parallel potential drops along auroral magnetic field lines produce positive gradients on electron distribution functions, $f(U_{||},U_{\perp})$ where, $U_{||}$ and $U_{\perp}$ are the parallel and perpendicular velocities of electrons, respectively [Gorney et al., 1985; Dusenbery and Lyons, 1982; Omidi and Gurnett, 1986; Omidi, et al., 1984]. Electron beams are associated with gradients $\frac{df}{dU_{||}} > 0$, and mirroring electrons with $\frac{df}{dU_{\perp}} > 0$. Electron energy losses in the atmosphere produce loss cones in the distribution functions. However, deep loss cones can also be produced in the absence of parallel electric fields if the charged particles are injected during short periods of time in long flux tubes such as flux transfer events which can generate dayside polar cusp aurora.

A common link exists among optical emissions, auroral hiss, and AKR. The link is the shape of the electron distribution functions. For instance, light emissions may take away parallel energy from the electrons thus leaving deep minima at small pitch angles (Wagner et al., 1984). This affects the AKR generation through mechanisms that depend on plasma instabilities associated with the gradients $\frac{df}{dU_{||}} > 0$ and $\frac{df}{dU_{\perp}} > 0$. Such mechanisms may also depend on each other. Consider the situations where the distributions with $\frac{df}{dU_{||}} > 0$ drives the bump-in-tail instability, and the distribution with $\frac{df}{dU_{\perp}} > 0$ drives the electron cyclotron maser instability. When the above instabilities operate simultaneously, they may cause diffusion in velocity space which tends to smooth out both gradients ($\frac{df}{dU_{||}}$ and $\frac{df}{dU_{\perp}}$) by filling with particles the velocity space between background (cold) and energetic electrons. If one of the instabilities has a faster growth rate, it can reduce both gradients and in the process suppress the other instability. Such effects account for temporal variations of AKR.

Auroral hiss, associated with precipitating electrons, is a whistler mode plasma emission with frequencies from 1kHz to the electron plasma frequency, ω_{pe}. In the dayside auroral zone, hiss may have components in the electron acoustic mode [Tokar and Gary, 1984]. Pottelette et al. (1987) presented observations where AKR is associated with impulsive broadband electrostatic hiss. In these cases the bursts of electrostatic waves are correlated with intense keV electron beams which cause AKR. An obvious interpretation of this association is that these electrostatic waves were generated by the electron acoustic instability. Thus one is naturally led to believe that the strong electrostatic turbulence from intense

electron beams may play a role in the AKR production and in discrete auroral processes. Pritchett and Winglee (1989) have shown that there should be electrostatic waves driven by bump-in-tail instability in association with AKR.

Another scenario involves the extent of AKR source regions along magnetic field line being associated with double layers. In that case the AKR source regions would be small in comparison to the latitudinal extent of discrete auroral forms in each auroral oval. In what follows, we will summarize the empirical and theoretical indirect evidence supporting the idea of localized parallel and/or transverse dimension of AKR source regions. Phenomenologically, discrete aurora, hiss, and AKR have magnetically conjugate sources. Whether there is a cause and effect relationship between them is not obvious. Nevertheless, such information can be considered as indirect evidence supporting the main conclusion of the present study, that AKR dependence on area of discrete aurora requires AKR sources to be localized and distributed uniformly in size over the average discrete auroral oval area.

Certain critical space experiments have been performed that provided some evidence regarding the small transverse size of AKR source regions. Some of the results need further confirmation as there is a sticky point related to the broad spectrum of derived transverse dimensions of AKR source regions. A few examples of observed localized AKR source regions are cited below. Calvert (1981b) reported AKR source characteristics as observed by the ISIS-1 satellite. Among other properties he listed thin sources distributed in altitude as a function of frequency, by using a simple refraction model. He concluded that observed AKR waves with the same frequency can originate at different altitudes or equivalently at different Ω_e and can arrive at one point by following different ray paths. This reasoning allows a hollow emission

cone to form around an AKR source region. The Viking satellite observed AKR source regions at altitudes between 6000 and 7000 km. Evidence for density depletions (plasma cavities) was found in the observed plasma structure (deFeraudy et al., 1987). Inside these source regions the above authors found the R-X AKR amplitude peaking at the local Ω_e, and possibly slightly below it. Furthermore, they found that the Z-mode amplitude inside the source region is much smaller that the R-X mode AKR amplitude. That supports our assumption that the observations used in this statistical study wre mainly R-X fundamental modes.

Some observations of AKR involving drift tones were interpreted by Gurnett and Anderson (1981) as due to shocklike structures moving up or down magnetic field lines with equal probability. These findings add to the indirect evidence that AKR source regions are localized in the parallel and the transverse direction as electrostatic shocks are thought to be localized in a similar way. Omidi and Gurnett (1982) predicted a hollow emission cone by computing growth rates occurring only in discrete intervals of Ω_e. However, they cautioned that more study is required before accepting as conclusive this result which corroborates the idea of Calvert (1981b) regarding the laser mechanism for AKR production. Baumback et al. (1986), using ISEE-1 and ISEE-2 as a wide base interferometer, inferred very small scale AKR source regions with a diameter less than about 10 km. This again means that the dimensions of AKR source regions both parallel and transverse to the magnetic field are limited to scales less than 10 km. It is important to establish the scale of the source size because it has serious implications on the validity of the electron cyclotron maser instability as an AKR generating mechanism. For instance, if AKR is simply amplified galactic background radiation as is tacitly assumed by Wu and Lee (1979) then for small scale source regions very high growth rates are required to explain the observed intensities. The required growth rates may be much greater

than those predicted by Wu and Lee (1979). Perhaps the coherent laser mechanisms proposed by Calvert (1982) can perform efficiently enough to explain the interferometric observations. More recently, Baumbeck and Calvert (1987) have inferred source sizes substantially less than the kilometric wavelength, therefore, they interpreted the wave generation to be a radio laser rather than an electron cyclotron maser. Our study cannot distinguish between laser and maser AKR production mechanisms but it establishes the dependence AKR power on the area of discrete aurora which requires localized acceleration regions for its generation.

In order to follow the theoretical developments of AKR generation based on properties of plasma in the AKR source regions, we will include a few examples of theories that assumed or predicted small scale sizes of the AKR source regions.. Omidi and Gurnett (1982) have shown that for a particular electron distribution function the ratio $(\omega-\Omega_e)/\Omega_e$ is small (10^{-3} to 10^{-2}) where growth rates are positive. Since $\omega>\Omega_e$ the relativistic resonance conditions $\omega-\Omega_e(1-\frac{V^2}{2C^2})^{1/2} = k_{||}U_{||}$ is satisfied for electrons with $k_{||}U_{||} > 0$. (Here, ω is the wave angular frequency Ω the electron gyrofrequency, U the particle velocity, $U_{||}$ the parallel electron velocity, and $k_{||}$ the parallel component of the propagation wave number.) Experiments have shown that the peak of the spectrum has a frequency of 250 kHz corresponding to a wavelength of about 1 km. In the above relation, if ω is to be close to Ω_e upon generation of the wave, the peak AKR waves must be generated at relatively low altitudes in the earth's magnetic field. Furthermore, the altitude extent of the source for a particular frequency has to be a thin layer. Combining the strong dependence of Ω_e on altitude with the resonance condition, one predicts an extended

source region with a range from 1.3 to 3.1 R_E geocentric distance or 2000 to 14000 km altitude range (corresponding to an AKR frequency span 50-700 kHz.) Clearly the first harmonic of the R-X mode follows an inverse relation with altitude. When downgoing, these electromagnetic waves are reflected at the right hand cutoff, which effectively blocks their observation at the earth's surface. Thus the AKR X-mode is bounded from below approximately by Ω_e. At one site the fundamental and its higher harmonics are generated in a region of small thickness along a field line. Of course the relative intensities of fundamental and second harmonic AKR depend on the ration ω_{pe}/Ω_e [Melrose et al., 1982; Winglee, 1985. a, b]. The fundamental X-mode growth dominates if $\omega_{pe}/\Omega_e \leq 0.3$, while the second harmonic X-mode growth dominates when $0.3 \leq \omega_{pe}/\Omega_e \leq 1$. Winglee and Pritchett (1986) have determined by linear growth rate analysis that the maser emissions can be more intense than electrostatic emissions only when $(n_E/n_b) \leq 0.8$ where, n_E is the density of the energetic electron component and n_b is the density of the cold background electron component. Unfortunately, observations show $n_E/n_b \geq 1$ in AKR source regions.

New theoretical results relevant to quasilocal AKR source regions were obtained by Pritchett and Winglee (1989). They performed two-dimensional electromagnetic particle simulations and three-dimensional ray-tracings in order to study generation, propagation and refraction of AKR in a dipolar magnetic field. In their simulations they found: (1) as ω_{pe}/Ω_e increases the efficiency of the maser instability decreases, (2) for a fixed ω_{pe}/Ω_e in an auroral cavity the maser instability develops over a short distance (20-30 km) along the magnetic field line, (3) the AKR produced by the instability has a wave packet structure whose spatial extent

along the field is only 4-6 km. All three of the above results are of localized nature. A simple uniform distribution of such localized events over discrete auroral areas is compatible with our statistical result that global AKR power is dependent upon the area of discrete aurora. From their ray-tracing analysis, Pritchett and Winglee (1989) found: (1) an amplification of about $10^{4.3}$ above background level can be achieved in a path length of less than 100 km, (2) such an amplification is completed within a distance of about 20 km along the magnetic field line. Again both of the above results have a quasi-local character which is consistent with out conclusion. The combination of the maser instability and the ray-tracing results support a maser instability mechanism which may operate in localized source regions producing AKR in narrow frequency bands of about 1kHz near the electron cyclotron frequency. Further support for this theory is found in discrete spectral structure of AKR observed by Gurnett et al. (1979) and Gurnett and Anderson (1981).

Most recently Wong et al. (1988, manuscript) have completed a study of the cyclotron maser instability, using electron energies less than 1 keV. They found that for second harmonics of X-mode it is not necessary to satisfy the relativistic doppler-shift cyclotron resonance conditions. Instead it can be satisfied for a broad range of ratios ω_{pe}/Ω_e regardless of electron energy. Wong et al. also state that the fundamental X-mode exists when electron energies exceed a certain threshold (say 1 keV) whereas, the second harmonic X-mode can exist with any intensity of the fundamental X-mode as long as $\omega_{pe}/\Omega_e < 0.2$. This result explains some of the observations in the present paper, where, AKR power is observed by the Hawkeye and ISEE-1 satellites at times when aurora is either weak or absent over a major part of the simultaneously observed discrete auroral oval. Such cases in our paper are consistent

with second harmonic R-X mode generation in regions endowed with electrons of energies below 1 keV which may be associated with aurora below the threshold of DMSP spectrophotometers.

SUMMARY AND CONCLUSIONS

Observations of kilometric wavelength power from ISIS-1, Hawkeye and ISEE-1 satellites were compared to the area of discrete aurora, estimated in about two thousand DMSP auroral images. First the ISIS-1 measurements provided a low-altitude snapshot of the auroral oval with high quality auroral light quantification. This was combined with high altitude AKR power measurements to make possible comparisons between total auroral oval emitted spectral power and the radio wave power. Such measurements are useful in determining the efficiency of AKR generation by auroral electrons. Second the Hawkeye data collected in regions high above the north pole were excellent for comparisons of total AKR power flux to the area of discrete aurora. It was found that the total power flux increased as the discrete auroral oval area increased. Finally the ISEE-1 AKR power data, collected high above the equator, after comparison with discrete auroral oval area, produced a result that was the same as that of Hawkeye's DMSP. This statistical result from the average stereoscopic viewing of the auroral acceleration regions (or AKR source regions) can be explained by assigning the following properties to the AKR source regions:

1. they are shallow and their altitude depends on radio frequency,

2. the power flux emitted by them has an upper limit (a saturation limit) which is reached rapidly,

3. the transverse extent of the plasma cavities is small in comparison to the auroral oval latitudinal extent and the plasma cavities are distributed nearly uniformly over the area of the discrete auroral oval.

AKR frequently exhibits temporal variations in time scales greater than three minutes (the resolution of the averaged data used). These fluctuations, which were averaged out in the large statistical samples above, are explainable by slow quenching and fast onsets of the AKR generation mechanism. There is a sizeable set of data in which AKR was present while optical emission was absent as determined by DMSP auroral scanning spectrophotometers. This result is consistent with recent claims that second harmonic AKR is generated by low energy (several hundred eV) electrons. Such suprathermal electrons in our study should mirror high above the atmosphere to minimize optical auroral emissions setting their power level below the threshold of DMSP spectrophotometers. The conclusions of this study are consistent with the predictions of the electron cyclotron maser mechanism and the actually observed spatial distributions of parallel potentials over the polar regions.

ACKNOWLEDGMENTS

This work was supported by NASA Grants NAG5-227, NAGW-1254, and by NSF Grants ATM 8521590, ATM 86-46122 and ATM 88-05819. One of us, N. A. Saflekos, would like to thank Drs. J. D. Menietti and H. K. Wong for many fruitful discussions.

REFERENCES

Anger, C. D., T. Fancott, J. McNally, and H. S. Kerr, *Appl. Opt.*, **12**, 1753, 1973.

Baumbeck, M. M., D. A. Gurnett, W. Calvert and S. D. Shawhan, Satellite interferometric measurements of auroral kilometric radiations, *Geophys. Res. Lett.*, **13**, 1105, 1986.

Baumbeck, M. M, and W. Calvert, The minimum bandwidths of auroral kilometric radiation, *Geophys. Res. Lett.*, **14**, 119, 1987.

Bendiktov, E. A., G. G. Getmenstev, Y. A. Sazonov and A. F. Taroson, Preliminary results of measurements of the intensity of distributed extra-terrestrial radio frequency emission at 725 and 1525 MHz, (in Russian), *Kosm. Issled.*, **3**, 614, 1965.

Benson, R. F., Auroral kilometric radiation: Wave modes, harmonics and source region electron density structures, *J. Geophys. Res.*, **90**, 2753, 1985.

Benson, R. F., and W. Calvert, ISIS-1 observations of the source of AKR, *Geophys. Res. Lett.*, **6**, 479, 1979.

Benson, R. F., W. Calvert and D. M. Klumpar, Simultaneous wave and particle observations in the auroral kilometric radiation source region, *Geophys. Res. Lett.*, **7**, 959, 1980.

Buchau, J., J. A. Whalen and S. -I. Akasofu, On the continuity of the auroral oval, *J. Geophys. Res.*, **75**, 7147, 1970.

Calvert, W., The signature of auroral kilometric radiations on ISIS-1 ionograms, *J. Geophys. Res.*, **86**, 76, 1981a.

Calvert, W., The auroral plasma cavity, *Geophys. Res. Lett.*, **8**, 919, 1981b.

Calvert, W., A feedback model for the source of auroral kilometric radiation, *J. Geophys. Res.*, **87**, 8199, 1982.

Chiu, Y. T., and M. Schulz, Self-consistent particle and parallel electrostatic field distributions in the magnetospheric-ionospheric auroral region, *J. Geophys. Res.*, **83**, 629, 1978.

Cogger, L. L., J. S. Murphree, S. Ismail, and C. D. Anger, *Geophys. Res. Lett.*, **4**, 1977, 413.

Dulk, G. A., Radio emission from the sun and stars, *Ann. Rev. Astron. Astrophys.*, **28**, 169, 1985.

Dusenbery, P. B., and L. R. Lyons, General concepts on the generation of auroral kilometric radiation, *J. Geophys. Res.*, **87**, 7467, 1982.

Eather, R. H., and S. B. Mende, Systematics in auroral energy spectra, *J. Geophys. Res.*, **77**, 660, 1972.

Eather, R. H., DMSP calibration, *J. Geophys. Res.*, **84**, 4134, 1979.

DeFeraudy, H., B. M. Pedersen, A. Bahnsen and M. Jespersen, Viking observations of auroral kilometric radiation from the plasmasphere to the night auroral oval source regions, *Geophys. Res. Lett.*, **14**, 511, 1987.

Freund, H. P., H. K. Wong, C. S. Wu and M. J. Xu, An electron cyclotron maser instability for astrophysical plasmas, *Phys. Fluids*, **26**, 2263, 1983.

Gallagher, D. L., and D. A. Gurnett, Auroral kilometric radiation: Time-averaged source locations, *J. Geophys. Res.*, **84**, 6501, 1979.

Gorney, D. J., Y. T. Chiu, and D. R. Croley, Jr., Trapping of ion conics by downward parallel electric fields, *J. Geophys. Res.*, **90**, 1985, 4205.

Green, J. L., D. A. Gurnett and R. A. Hoffman, A correlation between auroral kilometric radiation and inverted-V electron precipitation, *J. Geophys. Res.*, **84**, 5216, 1979.

Green, J. L., N. A. Saflekos, D. A. Gurnett and T. A. Potema, A correlation between auroral kilometric radiation and field-aligned currents, *J. Geophys. Res.*, **87**, 10463, 1982.

Gurnett, D. A., The earth as a radio source, terrestrial kilometric radiation, *J. Geophys. Res.*, **79**, 4227, 1974.

Gurnett, D. A., High latitude electromagnetic plasma wave emissions in high latitude space plasma physics, B. Hultqvist and T. Hagfors - editors, Plenum, New York, NY, 355, 1983.

Gurnett, D. A., and R. R. Anderson, The kilometric radio emission spectrum relation to auroral acceleration process in physics of auroral arc formation, *Geophys. Monogr. Ser.*, Vol. **25**, S. -I. Akasofu and J. R. Kan - editors, AGU, Washington, DC, 341, 1981.

Gurnett, D. A., R. R. Anderson, F. L. Scarf, R. W. Fredricks and E. J. Smith, Initial results from ISEE-1 and 2 plasma wave investigation, *Space Sci. Rev.*, **23**, 103, 1979.

Gurnett, D. A., and J. L. Green, On the polarization and origin of auroral kilometric radiation, *J. Geophys. Res.*, **83**, 689, 1978.

Gurnett, D. A., and R. R. Shaw, Electromagnetic radiation trapped in the magnetosphere above the plasma frequency, *J. Geophys. Res.*, **78**, 8136, 1973.

Gurnett, D. A., S. D. Shawhan and R. R. Shaw, Auroral Hiss, Z-model radiation and auroral kilometric radiation in the polar magnetosphere: DE-1 observations, *J. Geophys. Res.*, **99**, 329, 1983.

Hewitt, R. G., and D. B .Melrose, Electron cyclotron maser emission near the cutoff frequencies, *Aust. J. Phys.*, **36**, 725, 1983.

Hewitt, R. G., D. B. Melrose and K. G. Ronnmark, The loss cone driven electron-cyclotron maser, *Aust. J. Phys.*, 35, 447, 1982.

Hoffman, R. A., R. A. Heelis and J. S. Prasad, A sun-aligned arc observed by DMSP and AE-C, *J. Geophys. Res.*, **90**, 9697, 1985.

Holzworth, R. H., J.-J. Berhtelier, D. K. Ullers, U. V. Fahleson, C.-G. Fälthammar, M. K. Hudson, L. Jalonen, M. C. Kelley, J. Kellogg, Tanskanen, M. Temerin and F. S. Mozer, The large-scale ionospheric electric field: Its variations with magnetic activity and relation to terrestrial kilometric radiation, *J. Geophys. Res.*, **82**, 2735, 1977.

James, H. G., Direction-of-arrival measurements of AKR and associated ELF data from ISIS-1, *G. Geophys. Res.*, **85**, 3367, 1980.

Kaiser, M. L., and J. K. Alexander, Terrestrial kilometric radiation, 3, Average spectral properties, *J. Geophys. Res.*, **82**, 3273, 1977.

Kaiser, M. L., J. K. Alexander, A. C. Riddle, J. B. Pierce and J. W. Warwick, Direct measurements by Voyager 1 and 2 of the polarization of terrestrial kilometric radiation, *Geophys. Res. Lett.*, **5**, 857, 1978.

LeQuéau, D. R., R. Pellat and A. Roux, The maser synchrotron instability in an inhomogenous medium, application to the generation of auroral kilometric radiation, *Ann. Geophys. Gauthier Villars*, **3**,, 273, 1985.

LeQuéau, D. R., R. Pellat and A. Roux, Direct generation of the auroral kilometric radiation by the maser synchrotron instability: An analytical approach, *Phys. Fluids*, **27**, 247, 1984a.

LeQuéau, D. R., R. Pellat and A. Roux, Direct generation of the auroral kilometric radiation by the maser synchrotron instability: Physical discussion of the mechanism and parametric study, *J. Geophys. Res.*, **89**, 2831, 1984b.

Lee, L. C., J. R. Kan and C. S. Wu, Generation of auroral kilometric radiation and the structure of the auroral acceleration regions, *Planet. Space Sci.*, **28**, 703, 1980.

Lee, L. C., and C. S. Wu, Amplification of radiation near cyclotron frequency due to electron population inversion, *Phys. Fluids*, **23**, 1348, 1980.

Melrose, D. B., K. G. Ronnmark and R. G. Hewitt, Terrestrial radiations: The cyclotron theory, *J. Geophys. Res.*, **87**, 5140, 1982.

Mende, S. B., and R. H. Eather, Spectroscopic determination of the characteristics of precipitating auroral particles, *J. Geophys. Res.*, **80**, 3211, 1975.

Mizera, P. F., and J. F. Fennel, Signature of electric fields from high and low altitude particle distribution, *Geophys. Res. Lett.*, **4**, 311, 1977.

Murphree, J. S., and C. D. Anger, On obsrevation of the instantaneous optical auroral distribution, *Can. J. Phys.*, **58**, 214, 1980.

Omidi, N., and D. A. Gurnett, Growth rate calculations of auroral kilometric radiations, *J. Geophys. Res.*, **87**, 2397, 1982.

Omidi, N., C. S. Wu and D. A. Gurnett, Generation of auroral kilometric radiation and Z-mode radiation by the cyclotron maser mechanism, *J. Geophys. Res.*, **89**, 883, 1986.

Omidi, N., and D. A. Gurnett, Path integrated growth of auroral kilometric radiations, *J. Geophys. Res.*, **89**, 10801, 1984.

Pritchett, P. L., Relativistic dispersion and the generation of auroral kilometric radiation, *Geophys. Res. Lett.*, **11**, 143, 1984a.

Pritchett, P. L., Relativistic dispersion, the cyclotron maser instability, and auroral kilometric radiation, *J. Geophys. Res.*, **89**, 8957, 1984b.

Pritchett, P. L., and R. J. Strangeway, A simulation study of kilometric radiation generation along an auroral field line, *J. Geophys. Res.*, **90**, 9650, 1985.

Pritchett, P. L., and R. M. Winglee, Generation and propagation of kilometric radiation in the auroral plasma cavity, *J. Geophys Res.*, **94**, 129, 1989.

Pottelette, R., and M. M. Malingre, Observations of intense electrostatic hiss bands in the source regions of auroral kilometric radiation, *Geophys. Res. Lett.*, **14**, 515, 1987.

Rees, M. H., and D. Luckey, Auroral electron energy derived from ratios of spectroscopic emissions, 1. Model computations, *J. Geophys. Res.*, **79**, 5181, 1974.

Saflekos, N. A., R. E. Shawhan, and R. L. Carovillano, Correlations of auroral kilometric radiation with visual auroras and with Birkeland currents in High-Latitude Space Plasma Physics, Eds. B. Hultqvist and T. Hagfors, Plenum Publ. Corp., 1983.

Shawhan, S. D., and D. A. Gurnett, Polarization measurements of auroral kilometric radiations by Dynamics Explorer-1, *Geophys. Res. Lett.*, **9**, 913, 1982.

Sheehan, R. E., R. L. Carovillano, and M. S. Gussenhoven, Occurrence and recurrence in auroral activity in DMSP images, *J. Geophys. Res.*, **87**, 3581, 1982.

Strangeway, R. J., Wave dispersion and ray propagation in a weakly relativistic electron plasma: Implications for the generation of auroral kilometric radiation, *J. Geophys. Res.*, **90**, 9675, 1985.

Tokar, R. L., and S. Gary, Electrostatic hiss and the beam-driven electron acoustic instability in the dayside polar cusp, *Geophys. Res. Lett.*, **11**, 1180, 1984.

Voots, G. R., D. A. Gurnett, S.-I. Akasofu, Auroral kilometric radiation as an indicator of auroral magnetic disturbances, *J. Geophys. Res.*, **82**, 2259, 1977.

Wagner, J. S., L. C. Lee, C. S. Wu and T. Tajima, Computer simulation of auroral kilometric radiation, *Geophys. Res. Lett.*, **10**, 483, 1983.

Wagner, J. S., L. C. Lee, C. S. Wu and T. Tajima, A simulation study of the loss cone driven cyclotron maser applied to auroral kilometric radiations, *Radio Sci.*, **19**, 509, 1984.

Winglee, R. M., Enhanced growth of whistlers due to bunching of utrapped electornis, *J. Geophys. Res.*, **90**, 5141, 1985a.

Winglee, R. M., Fundamental and harmonic electron cyclotron maser emission, *J. Geophys. Res.*, **90**, 9663, 1985b.

Winglee, R. M., and P. L. Pritchett, The generations of low-frequency electrostatic waves in association with auroral kilometric radiation, *J. Geophys. Res.*, **91**, 13531, 1986.

Wong, H. K., D. Krauss-Varban and C. S. Wu, On the role of the energy of suprathermal electrons in the generation of auroral kilometric radiations, manuscript, 1989.

Wong, H. K., C. S. Wu, F. J. Ke, R. S. Schneider an L. F. Ziebell, Electromagnetic cyclotron-loss-cone instability assoicated with weakly relativistic electrons, *J. Plasma Phys.*, **28**, 503, 1982.

Wu, C. S., Lin, H. K. Wong, S. I. Tsai and R. L. Zhou, Absorption and emission of extraordinary mode electromagnetic waves near cyclotron frequency in non-equilibrium plasmas, *Phys. Fluids*, **24**, 2191, 1981b.

Wu C. S., and L. C. Lee, A theory of terrestrial kilometric radiations, *Astrophys. J.*, **230**, 621, 1979.

Wu, C. S., S. T. Tsai, M. J. Xu and J. W. Shen, Saturation and energy conversion efficiency of auroral kilometric radiation, *Astrophys. J.*, **248**, 394, 1981a.

Wu, C. S., H. K. Wong, D. J. Gorney and L. C. Lee, Generation of the auroral kilometric radiation, *J. Geophys. Res.*, **87**, 4476, 1982.

Zarka, D. LeQuéau and F. Genova, The maser synchrotron instability in an inhomogeneous medium determination of the spectral intensity of auroral kilometric radiation, *J. Geophys. Res.*, **91**, 13542, 1986.

FIGURE CAPTIONS

Figure 1

Top panel shows the 3914Å data from the 7412160612UT pass. The clock dial is corrected geomagnetic latitude and corrected geomagnetic local time. the grey shade shows highest intensitivities in white. A series of white triangles near the noon meridian indicate the 100 km projected satellite track. The large illuminated area below 74° on the noon side is due to scattered daylight. Bottom left panel shows the Q=1 statistical auroral oval in corrected geomagnetic coordinates of latitude and local time. Calculated boundaries of the instantaneous aurora are indicated by connected triangles on the poleward and equatorward side of the oval. Bottom right cartesian plots show magnetic local time plots of the ratio of intensities of 5577Å over 3914Å. The bars indicate the standard error for the average ratio for emissions confined between the instantaneous auroral boundaries. The lower cartesian plot of intensity versus MLT shows the intensity in kR for the average 5577 and 3914Å along with the peak 3914Å intensity (Figure 1 is adapted from Murphree and Anger, 1980, Figures 2, 4 and 5).

Figure 2

Time plot of Hawkeye AKR power flux for December 16, 1974 from 0613 to 0626 UT. Power flux normalized to 7 earth radii distance with source at the earth's center.

Figure 3

Schematic view of noon-midnight meridional cross-sections of AKR propagation regions with sources above the plasmasphere between 70° and 76° invariant latitude from Gallagher and Gurnett (1979).

Figure 4

Top panel shows AKR electric field (dB) for four different frequencies as measured by an ISEE-1 satellite on January 22, 1979. Bottom panel shows a projection of the ISEE orbit in the Y-Z plane of solar magnetic coordinates (SM). UT and SM latitude are also indicated in the plot. The three filled triangles indicate times of simultaneous observations of AKR (dashed vertical lines) in the top panel. The different dashed lines correspond to times of instantaneous snapshots of the aurora from DMSP satellites shown in succeeding figures.

Figure 5

North hemisphere DMSP image (orbit 3781) on January 22, 1979 around 1258 UT. In the corrected geomagnetic latitude and local time, shown are discrete (black) and diffuse (stippled) aurorae. Bottom panel shows time plot of the AE index with vertical dashed lines corresponding to simultaneous observations of AKR power flux shown in Figure 4.

Figure 6

North hemisphere DMSP images for orbits 3782 and 12236 on January 22, 1979, around 1437 and 1425 UT. Discrete (black) and Diffuse (stippled) aurorae are coincident with AKR observations in Figure 4. In these two images one sees changes of area of discrete aurora in times as short as 12 minutes.

Figure 7

A sequence of DMSP images with relatively high temporal resolution involving delays of 4, 7, and 11 minutes. In going from DMSP orbit 12238 at 1750 UT to 8454 at 1754 UT and to 3784 at 1801 UT we see very small area of discrete aurora growing into arcs and finally into a westward traveling surge. Simultaneous AKR measurements are shown in Figure 4. It is interesting to note that the highest frequencies lead the lowest frequencies in succession as the discrete auroral area increases.

Figure 8a

Simultaneous ISEE-1 AKR power flux normalized to $7R_E$ and DMSP active aurora observations plotted in ISEE radial distance versus ISEE SM latitude. Top (bottom) row corresponds to 300 kHz (178 kHz) AKR, respectively. Left, middle, and right columns correspond to power fluxes $P_7 \geq 1^{-14}$, $10^{-15} \geq P_7 \geq 10^{-17}$, and $P_7 \leq 10^{-18}$ W m^{-2} Hz^{-1}, respectively.

Figure 8b

The same as Figure 8a except for moderate aurora.

Figure 8c

The same as Figure 8a except for frequencies 100 and 50 kHz.

Figure 8d

The same as Figure 8a except for moderate aurora and frequencies 100 and 50 kHz.

Figure 9

Frequency distribution of the number of DMSP images versus instantaneous ISEE AKR power fluxes. The simultaneous events are separated into bins by AKR angular frequency and by auroral activity. At the lowest power fluxes there are more moderate auroral images than active, for all AKR frequencies. At the highest power fluxes there are more active auroral images than moderate. At intermediate power fluxes there are more active auroral images than moderate, with the 100 kHz frequency category having the largest difference between numbers of active and moderate auroral images.

Figure 10

Simultaneous 3 min. average AKR power flux measurements from Hawkeye (dots in upper panels) and all-sky camera photographs taken every minute near local midnight in the auroral zone by the AFGL flying observatory (strips below AKR plots). Data covers a 2 hour interval from 0900-1100 UT on January 10, 1975.

Figure 11

North hemisphere DMSP image (orbit 3816) along with coincidental HAWKEYE AKR power flux normalized $7R_E$, and AE index. Labels in the image refer to the 2200 and 2400 corrected geomagnetic local time (CGLT) meridians and the 70° to 80° circles of constant corrected geomagnetic latitude (CGLAT). The vertical time scale at the left gives the universal time (HHMM) of the dawn-dusk scans recorded in the image on the right. Bars indicating the Hawkeye AKR power flux are plotted at the midpoint of the 3 min. averaging interval. Inset showing the AE index versus UT is marked with a vertical line at the approximate DMSP image universal time.

Figure 12

DMSP orbit 6784 on August 12, 1974. Figure 12 is similar to Figure 11 except for active aurora.

Figure 13

DMSP orbit on September 12, 1974. Figure 13 is similar to Figure 11 except for active aurora.

Figure 14

A scatter plot of Hawkeye AKR power fluxes versus DMSP auroral activity for a large sample of simultaneous observations. Several cases of AKR observations above 10^{-17}W-m^{-2}- Hz^{-1} power flux occurred at times of no auroral activity within the viewing regions of DMSP. The largest number of points per decade of power flux belongs to the M category.

Figure 15

The maximum power flux points versus auroral activity from Figure 14. A trend, from low to high power flux values is apparent as auroral activity strengthens from N to A. A decompressed scale would show an exponential increase of maximum power versus latitudinal width of an east/west widely pread discrete aurora.

Figure 16

Approximately one thousand DMSP images correlated with Hawkeye AKR power flux. The distribution of number of images versus power flux in three separate area categories (small, medium and large) are shown. The largest number of images in the lowest power flux decade appeared in the small area category. In contrast the fewest images in the lowest power decade occurred in the large area category. This relationship is inverted in the power flux decade from 10^{-15} to 10^{-14}W $m^{-2}Hz^{-1}$. The medium discrete auroral area category is nearly trimoidal consisting of events like those in small area, large area, as well as a third peak in the decade 10^{-18} to 10^{-17}W-m^{-2}-Hz^{-1} characteristic of the medium area discrete aurora. These distributions show clearly a dependence of AKR power flux on area of discrete aurora.

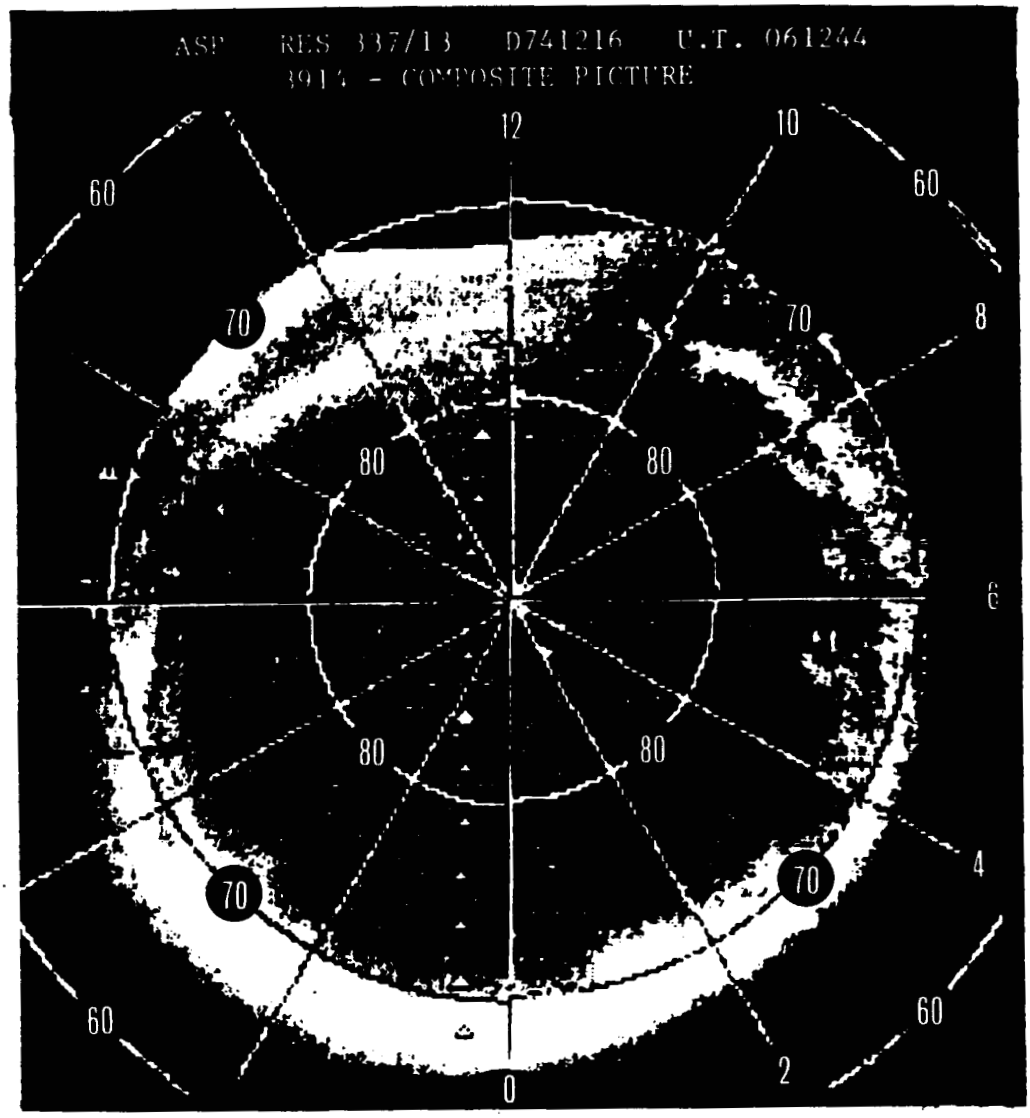

**ORIGINAL PAGE IS
OF POOR QUALITY**

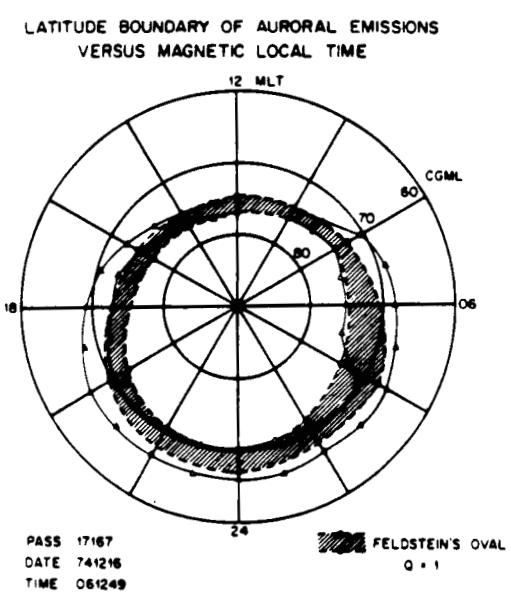

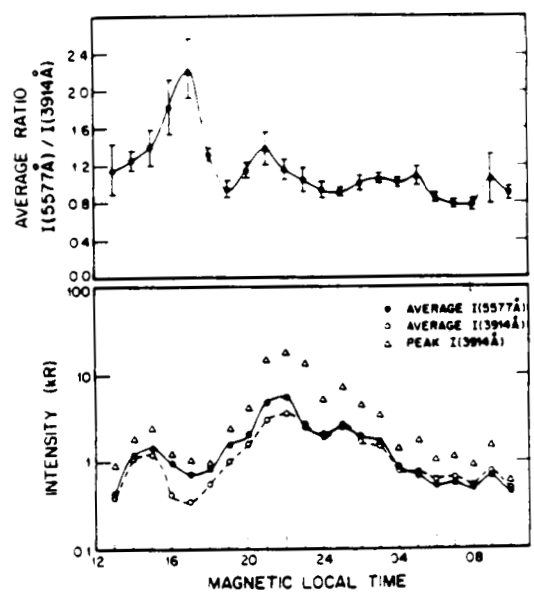

FIGURE 1

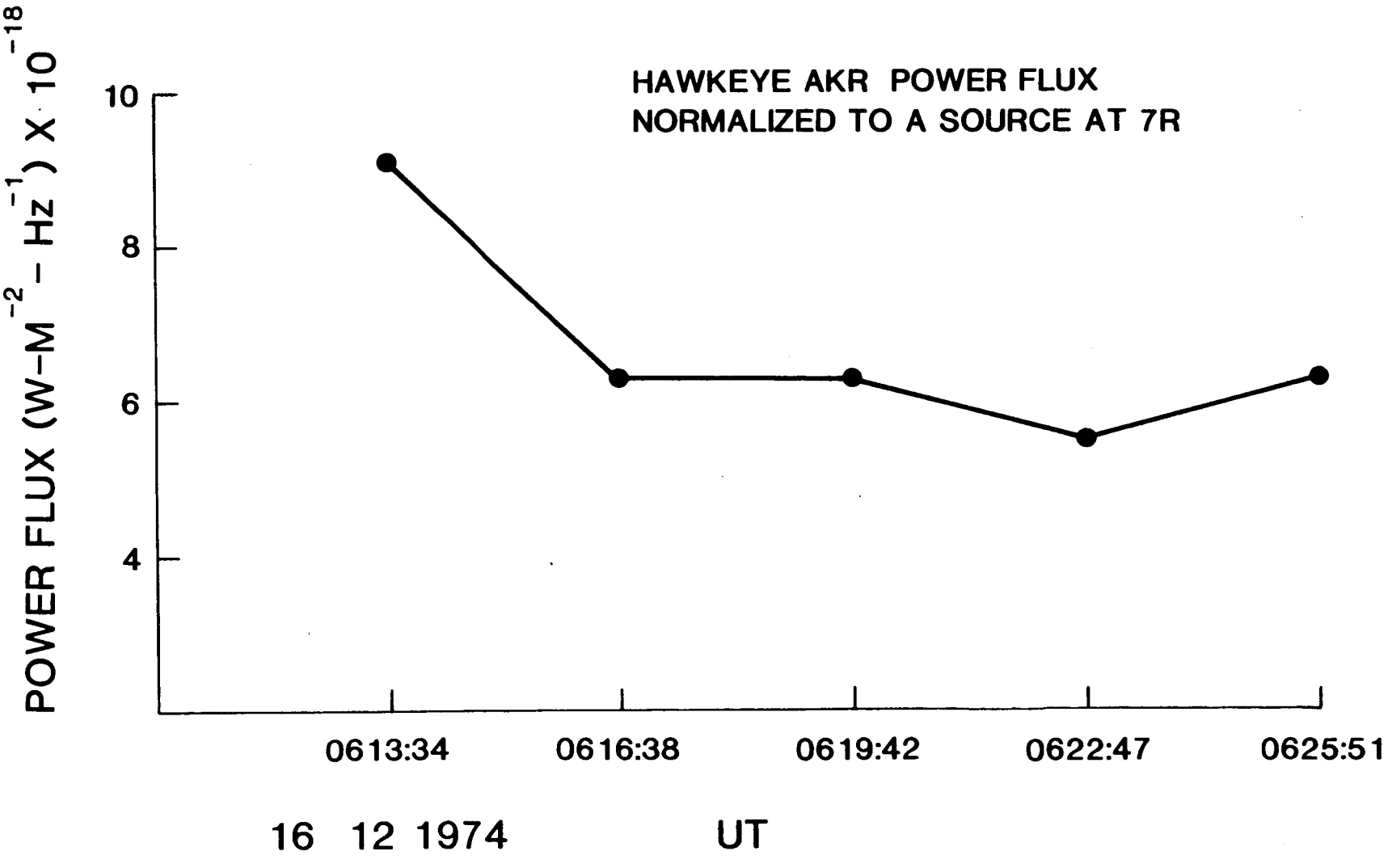
HAWKEYE AKR POWER FLUX
NORMALIZED TO A SOURCE AT 7R
POWER FLUX (W-M^{-2} - Hz^{-1}) X 10^{-18}
10
8
6
4
0613:34
0616:38
0619:42
0622:47
0625:51
16 12 1974
UT

FIGURE 2

ORIGINAL PAGE IS
OF POOR QUALITY

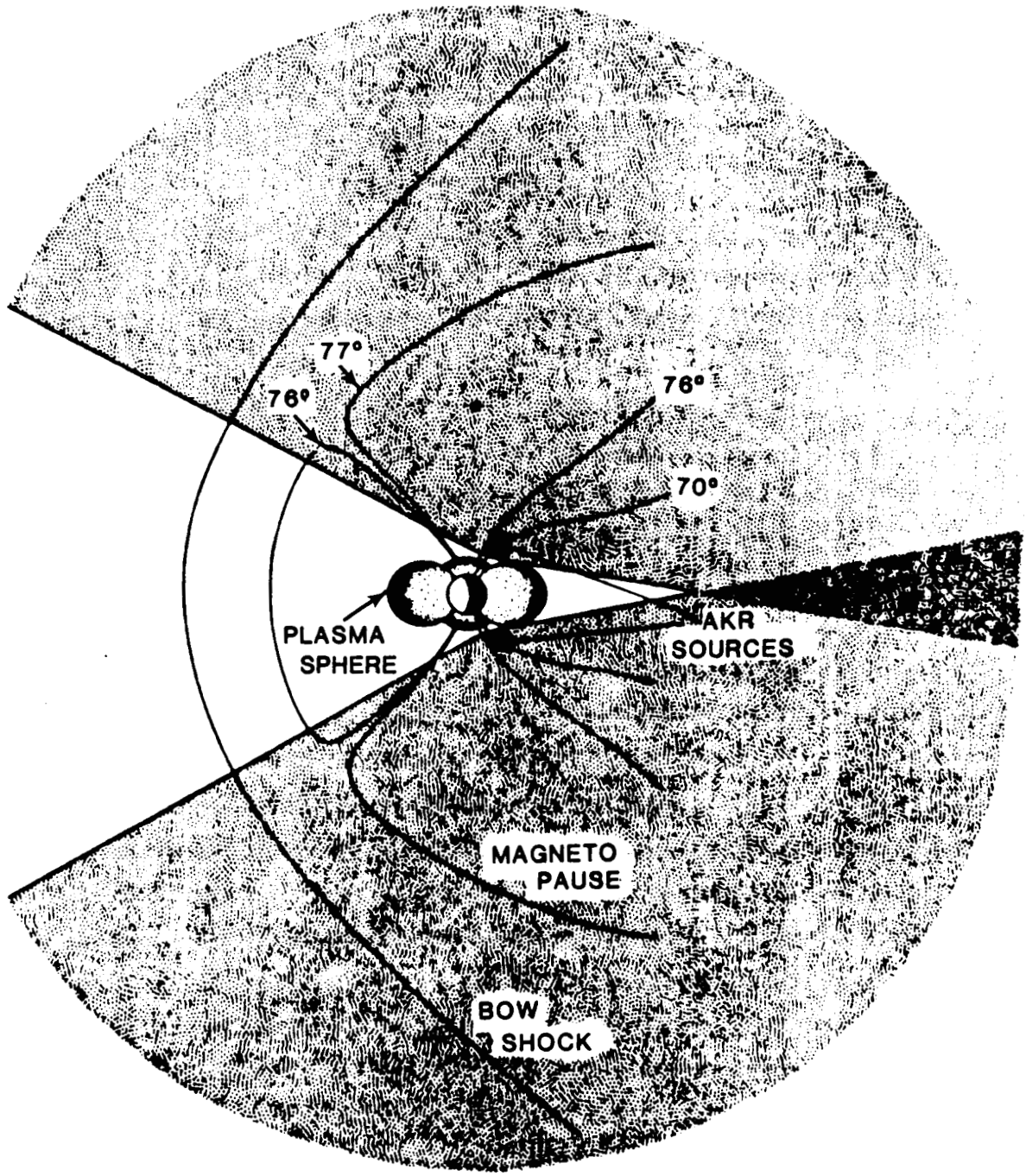

FIGURE 3

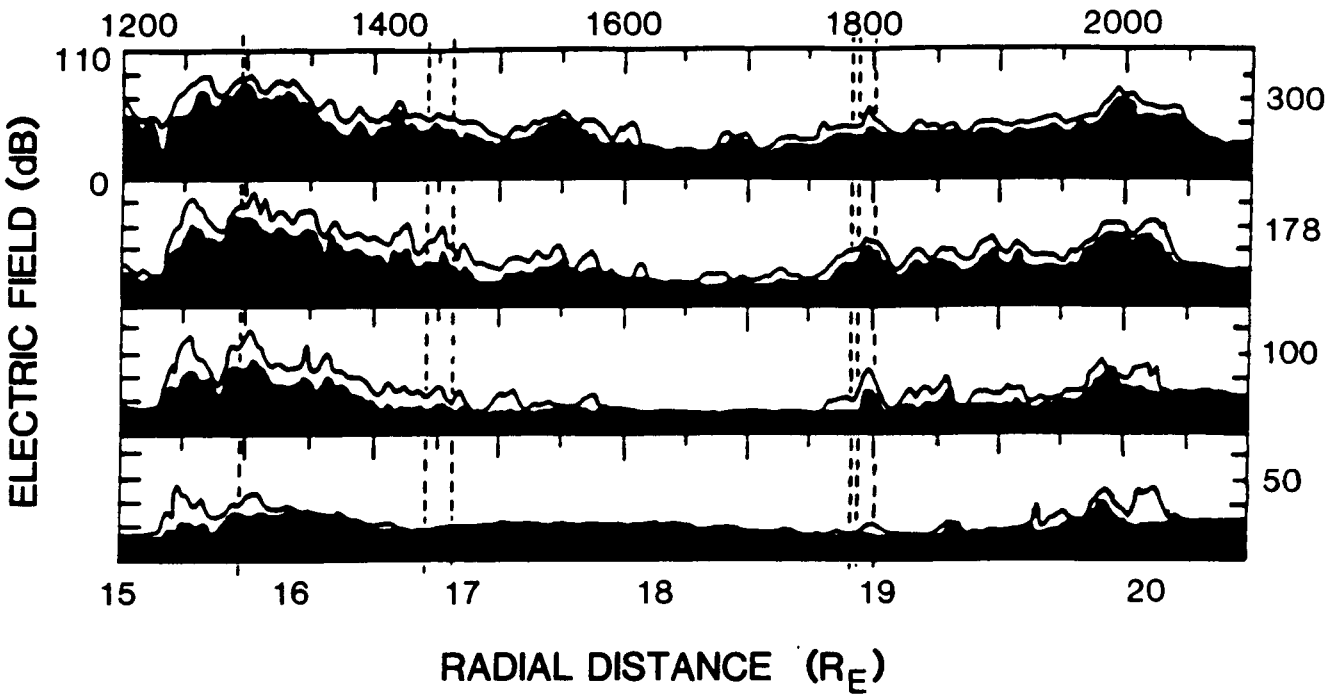
UNIVERSAL TIME
JAN 22, 1979
1200
1400
1600
1800
2000
110
0
300
178
100
50
ELECTRIC FIELD (dB)
15
16
17
18
19
20
RADIAL DISTANCE (R_E)

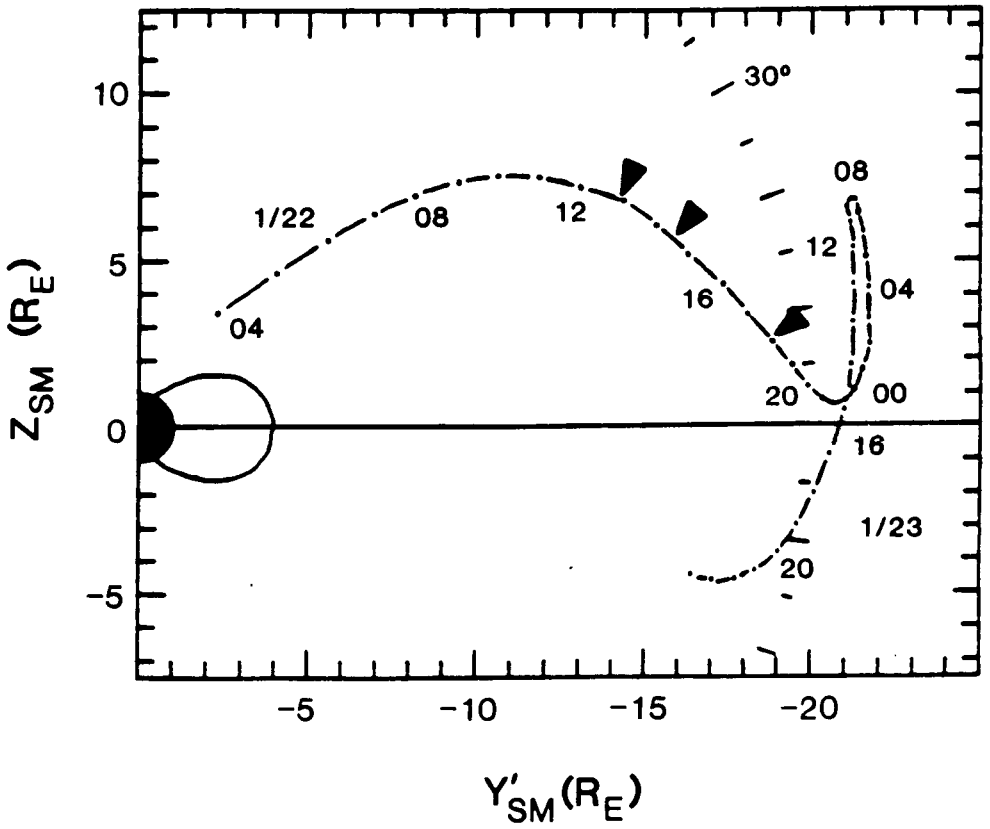
10
5
0
-5
Z_{SM} (R_E)
30°
1/22
08
12
16
20
00
04
08
12
04
16
1/23
20
-5
-10
-15
-20
Y'_{SM}(R_E)

FIGURE 4

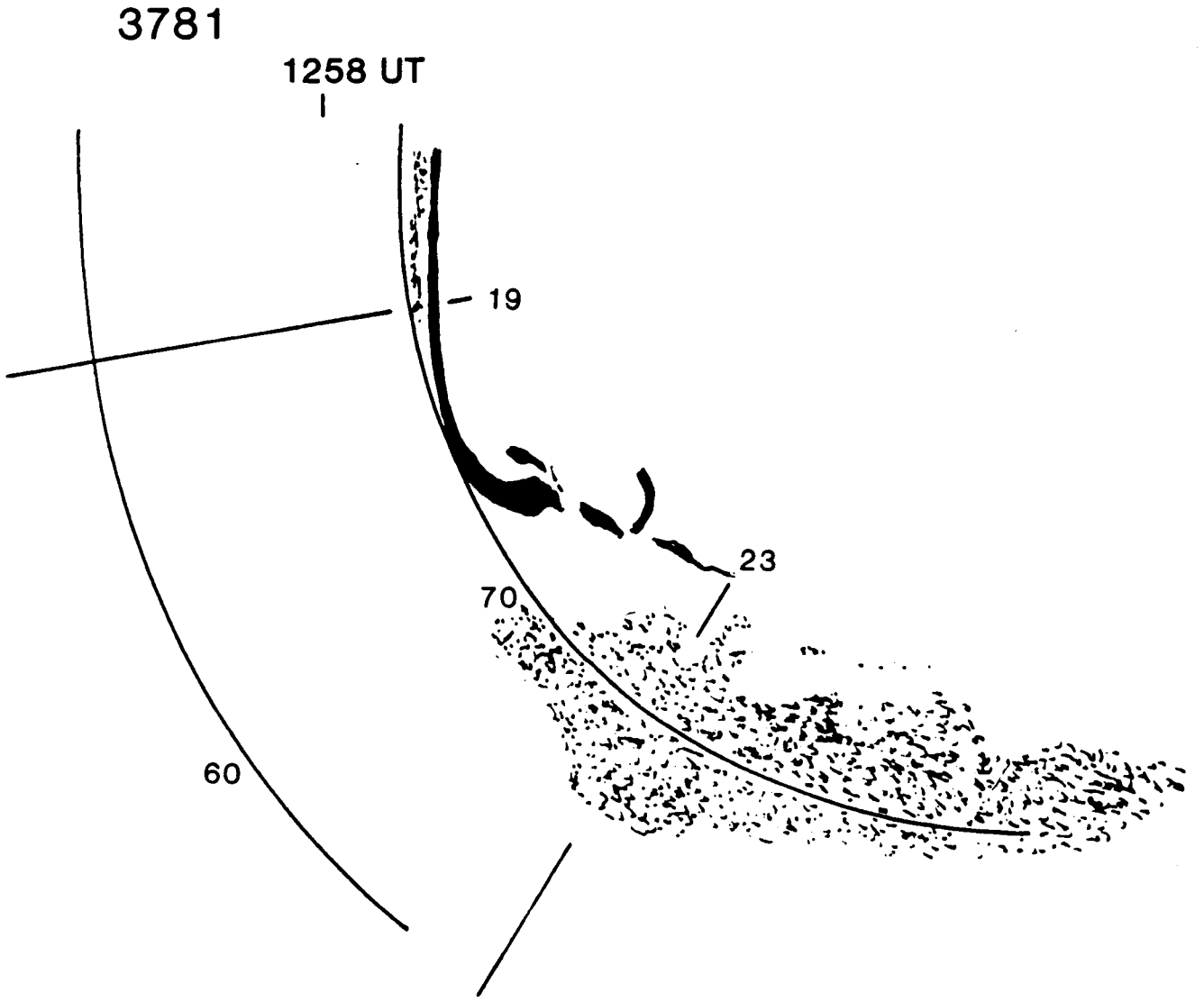

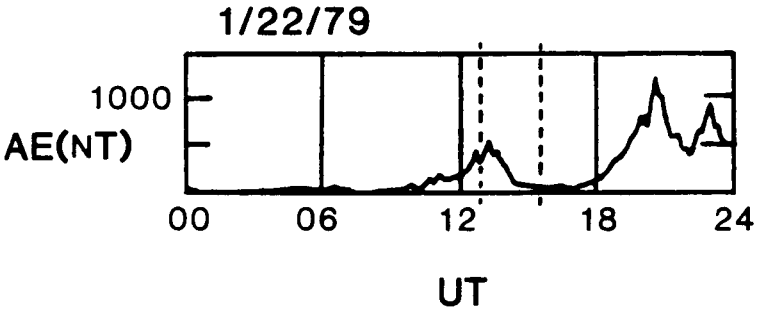

FIGURE 5

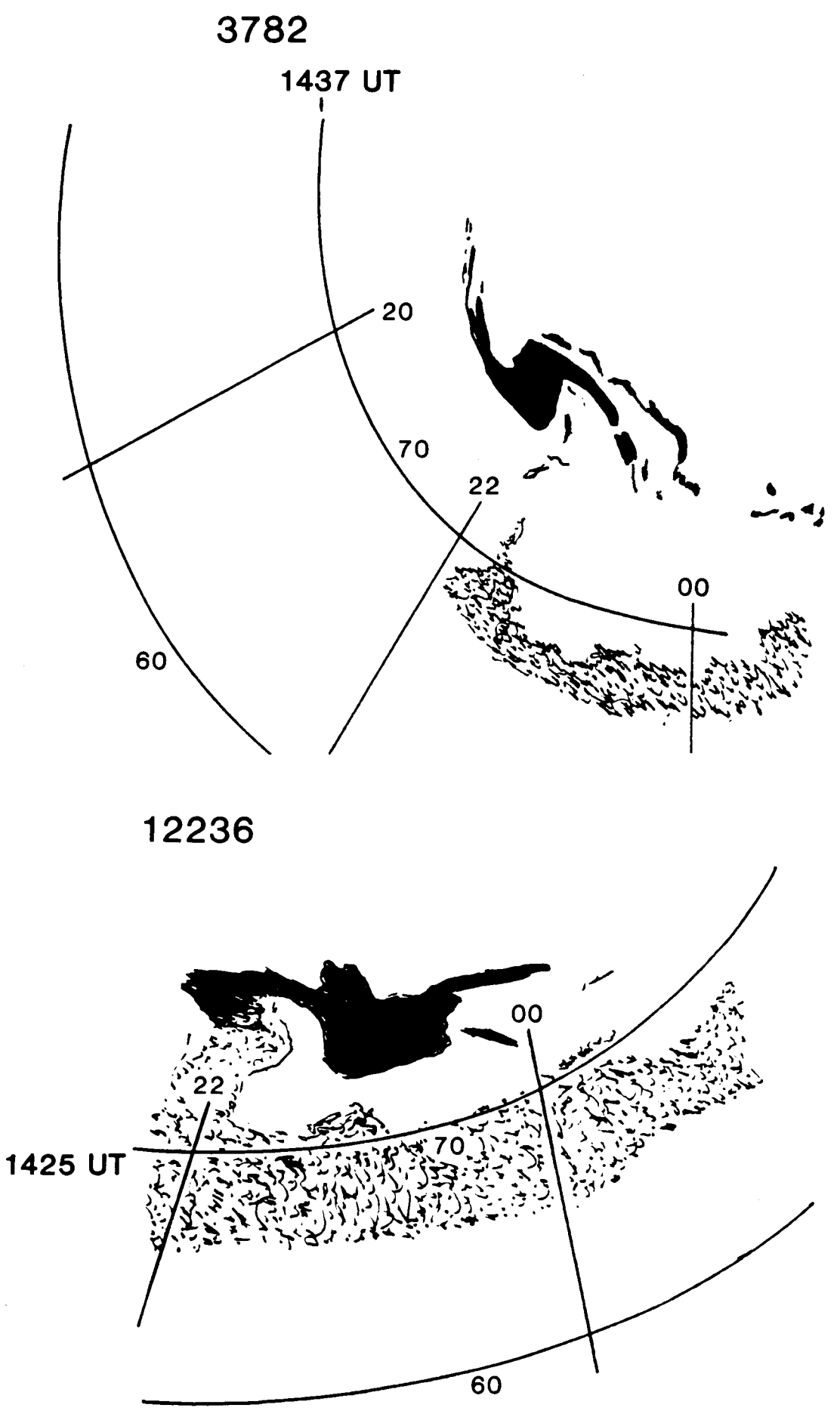

FIGURE 6

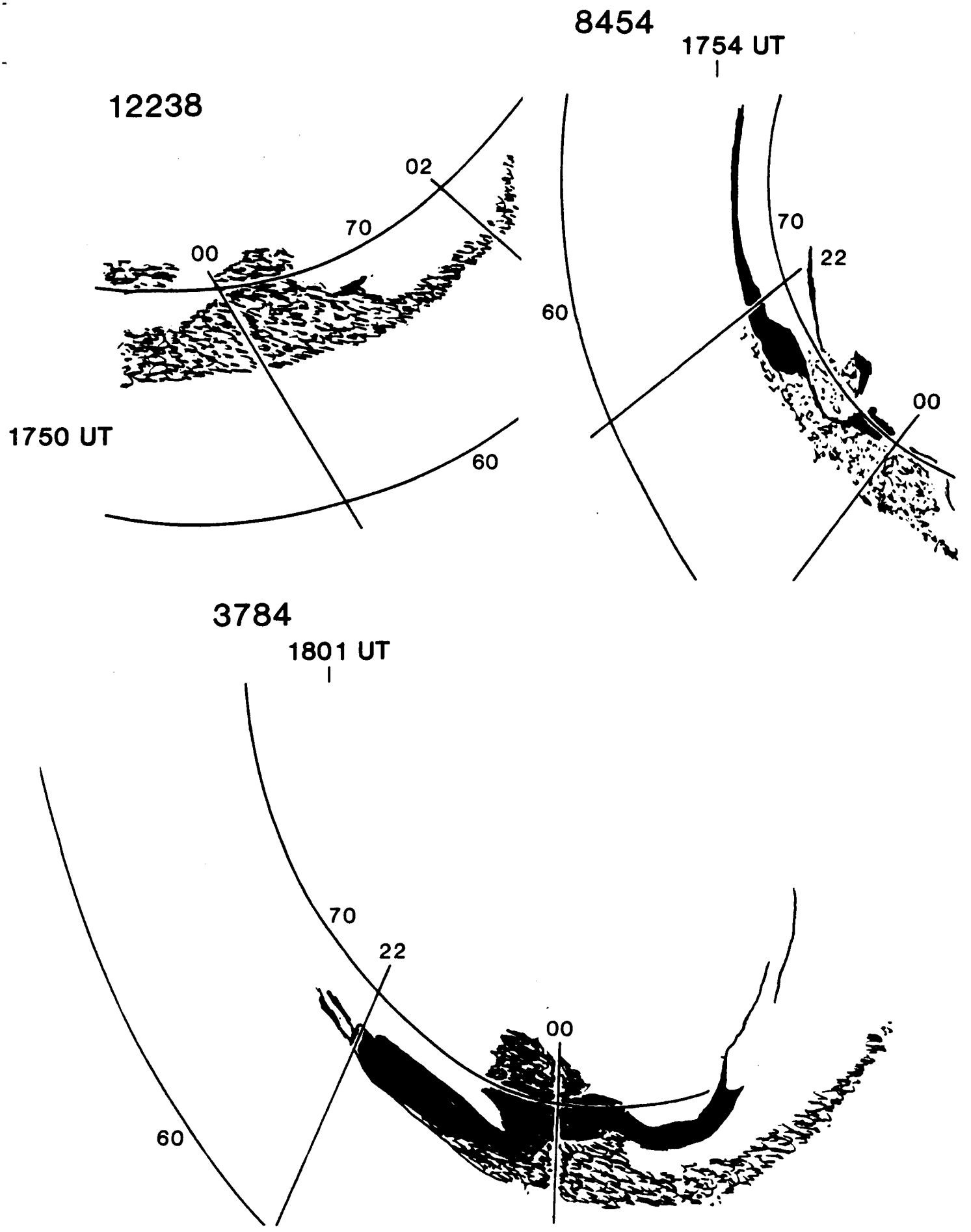
12238
02
70
00
1750 UT
60
8454
1754 UT
70
22
60
00
3784
1801 UT
70
22
00
60

FIGURE 7

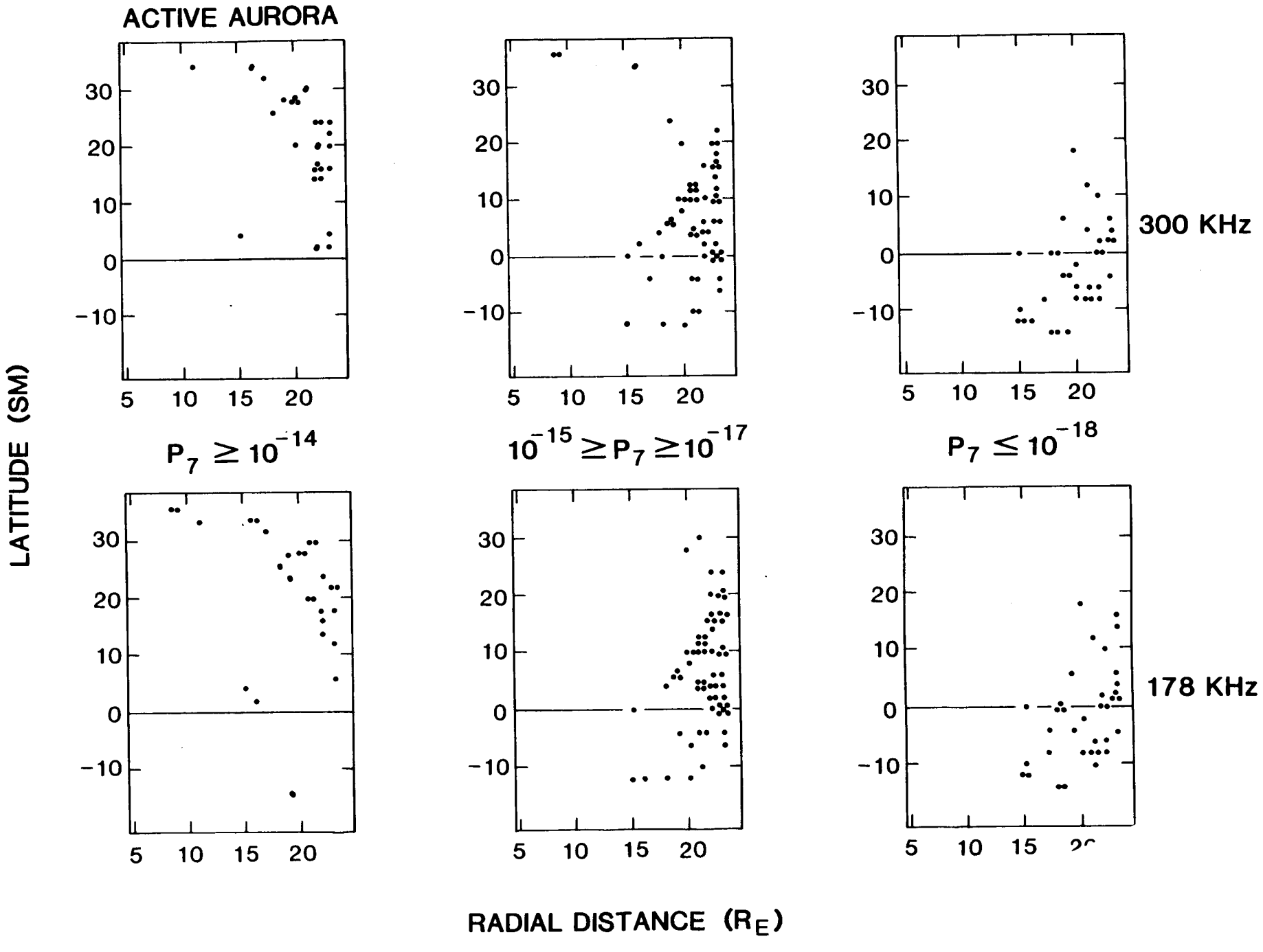
ACTIVE AURORA
30
20
10
0
-10
5
10
15
20
$P_7 \geq 10^{-14}$
$10^{-15} \geq P_7 \geq 10^{-17}$
$P_7 \leq 10^{-18}$
300 KHz
178 KHz
LATITUDE (SM)
RADIAL DISTANCE (R_E)

FIGURE 8a

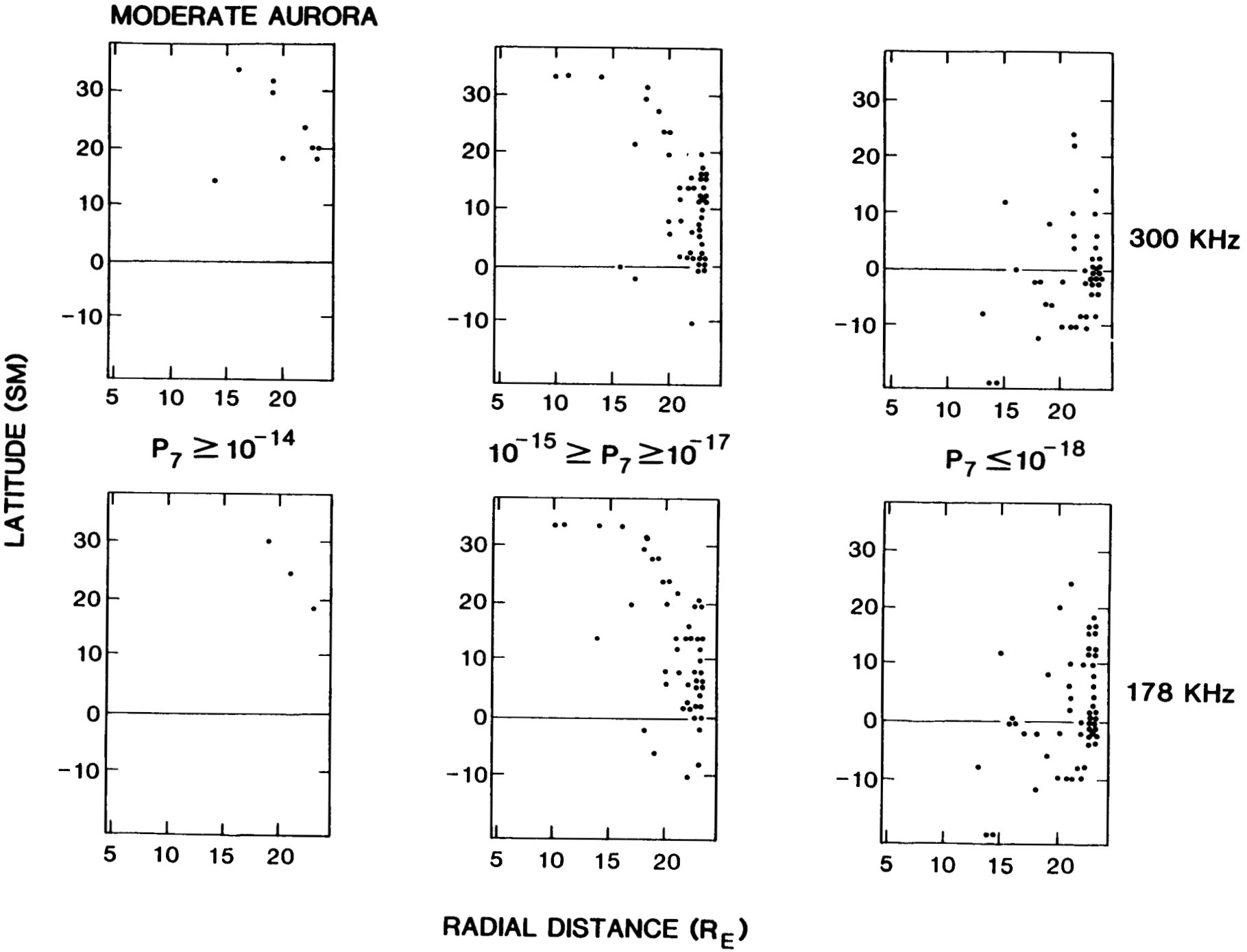
MODERATE AURORA
LATITUDE (SM)
30
20
10
0
-10
5
10
15
20
$P_7 \geq 10^{-14}$
$10^{-15} \geq P_7 \geq 10^{-17}$
$P_7 \leq 10^{-18}$
300 KHz
178 KHz
RADIAL DISTANCE (R_E)

FIGURE 8b

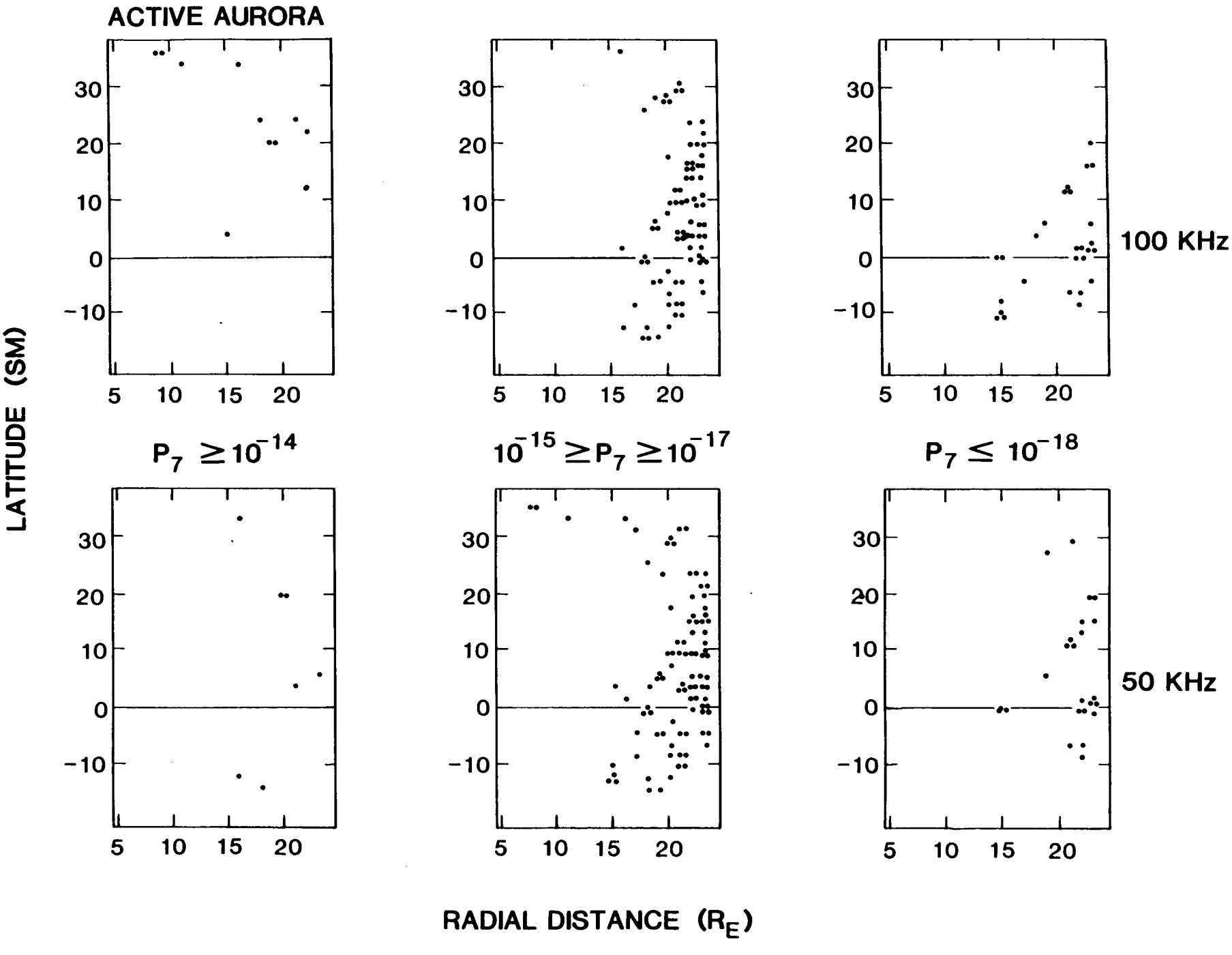
ACTIVE AURORA
LATITUDE (SM)
30
20
10
0
-10
5
10
15
20
$P_7 \geq 10^{-14}$
$10^{-15} \geq P_7 \geq 10^{-17}$
$P_7 \leq 10^{-18}$
100 KHz
50 KHz
RADIAL DISTANCE (R_E)

FIGURE 8c

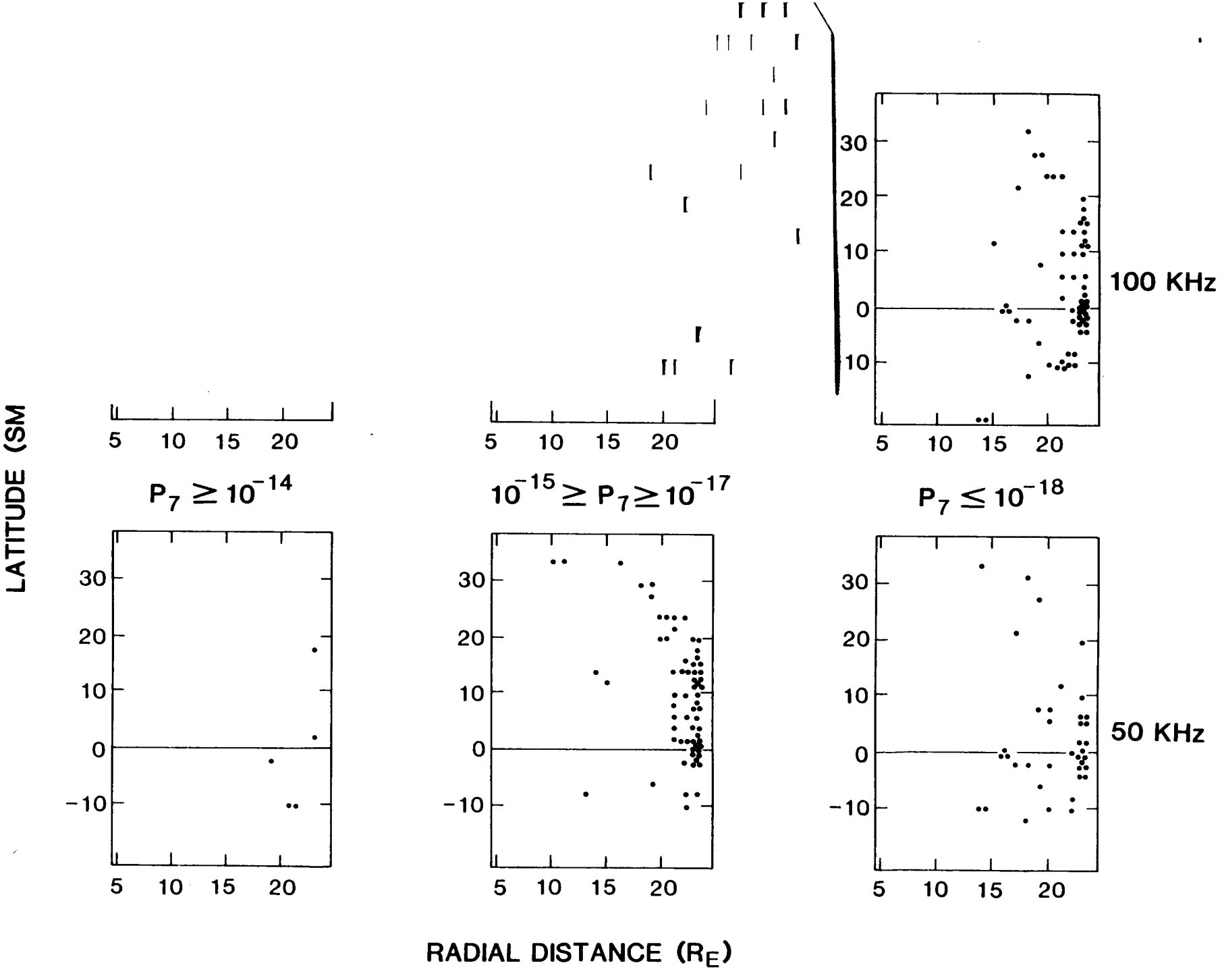
LATITUDE (SM
$P_7 \geq 10^{-14}$
$10^{-15} \geq P_7 \geq 10^{-17}$
$P_7 \leq 10^{-18}$
100 KHz
50 KHz
RADIAL DISTANCE (R_E)

Figure 8d

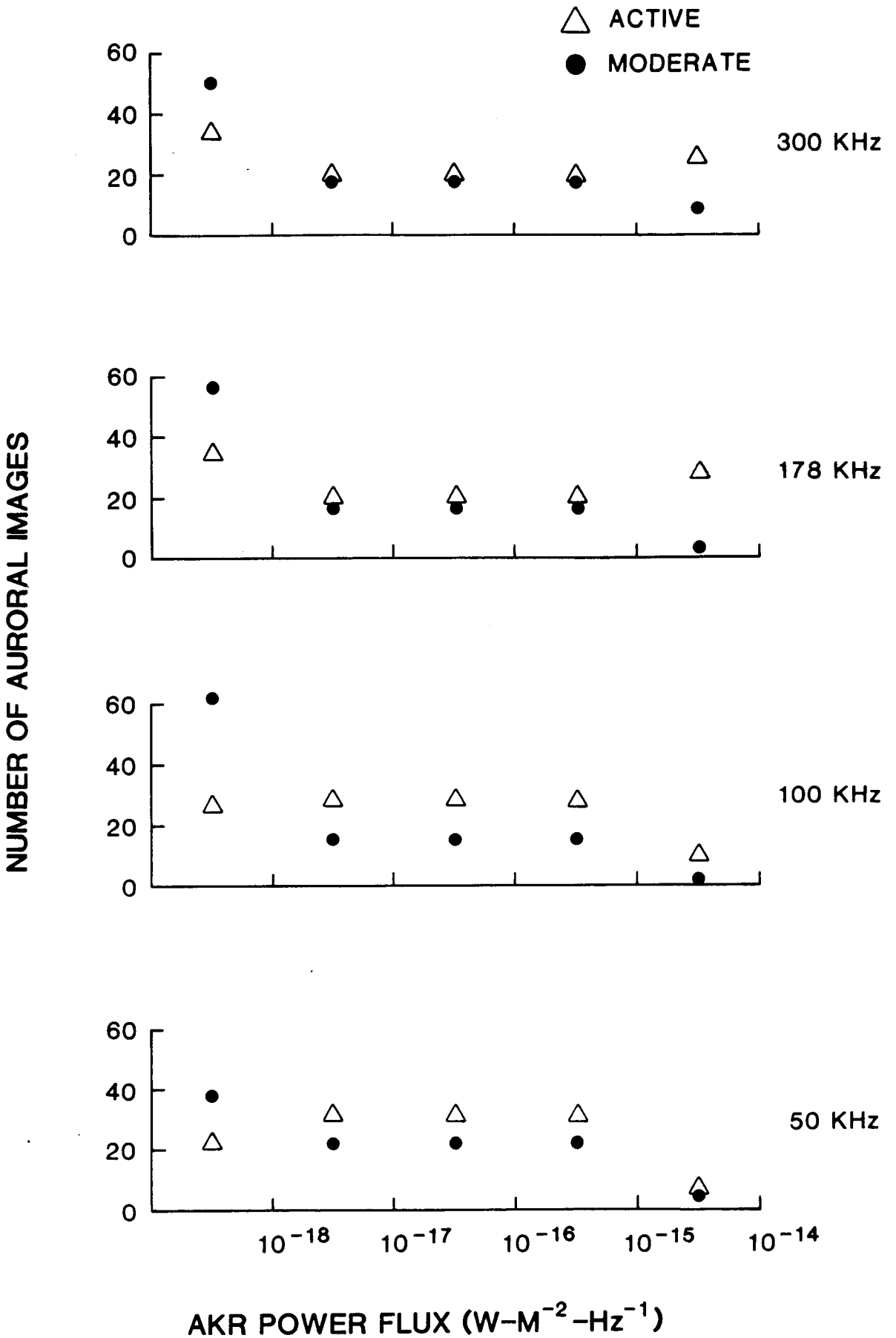
ACTIVE
MODERATE
300 KHz
178 KHz
100 KHz
50 KHz
60
40
20
0
NUMBER OF AURORAL IMAGES
10^{-18}
10^{-17}
10^{-16}
10^{-15}
10^{-14}
AKR POWER FLUX ($W-M^{-2}-Hz^{-1}$)

FIGURE 9

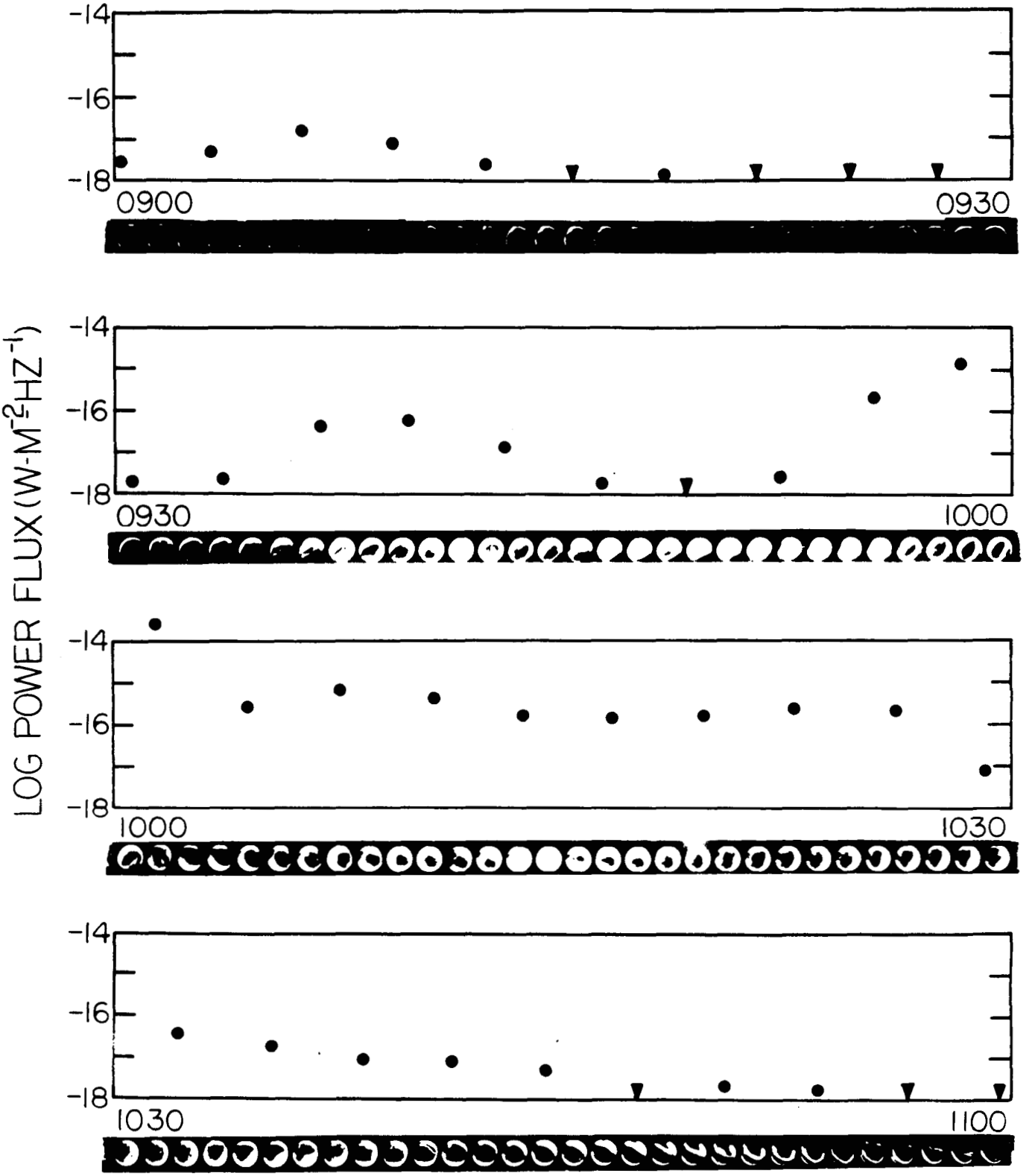
JAN 10, 1975
-14
-16
-18
0900
0930
0930
1000
1000
1030
1030
1100
LOG POWER FLUX (W-M^{-2}HZ^{-1})
UNIVERSAL TIME

FIGURE 10

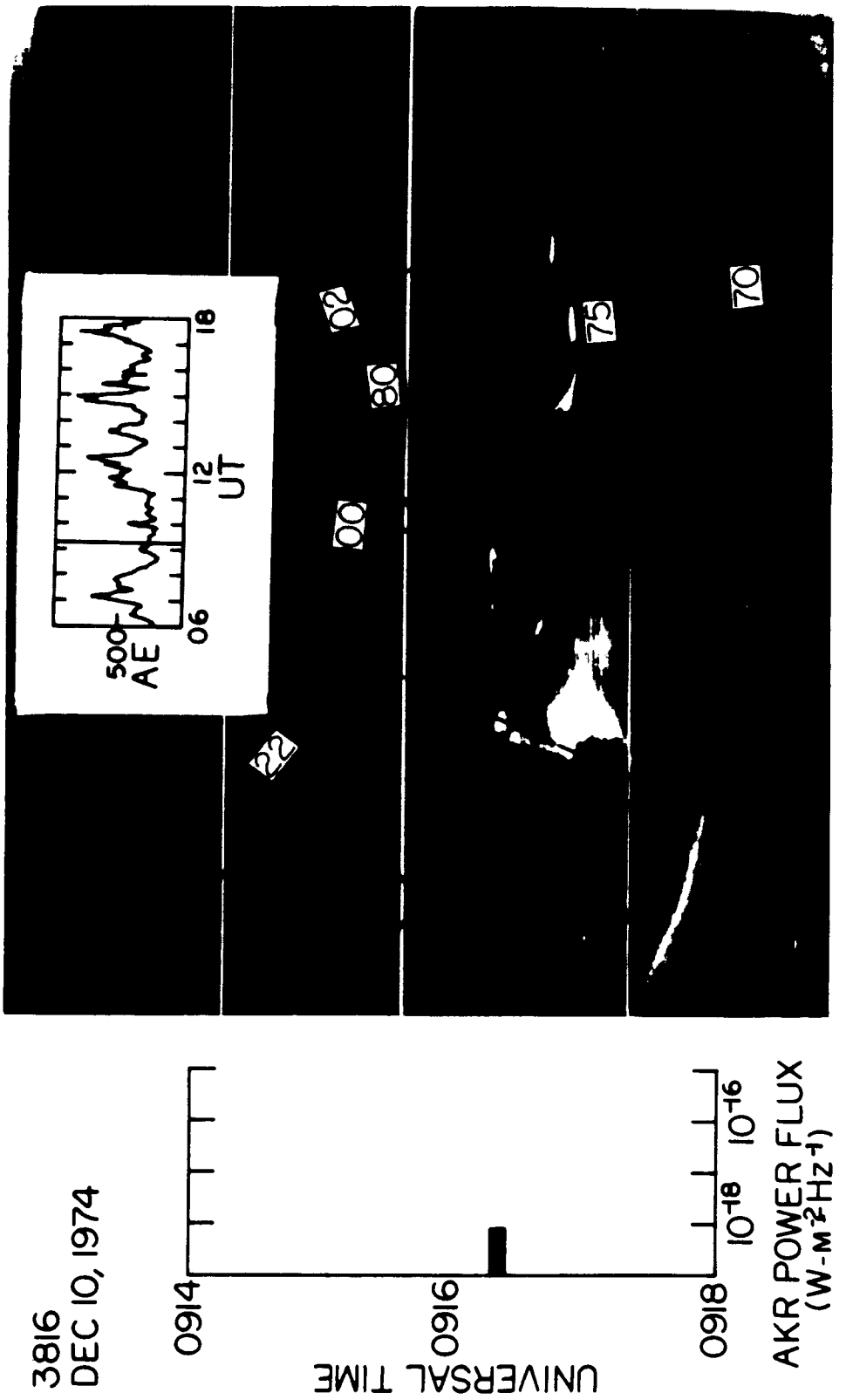

FIGURE 11

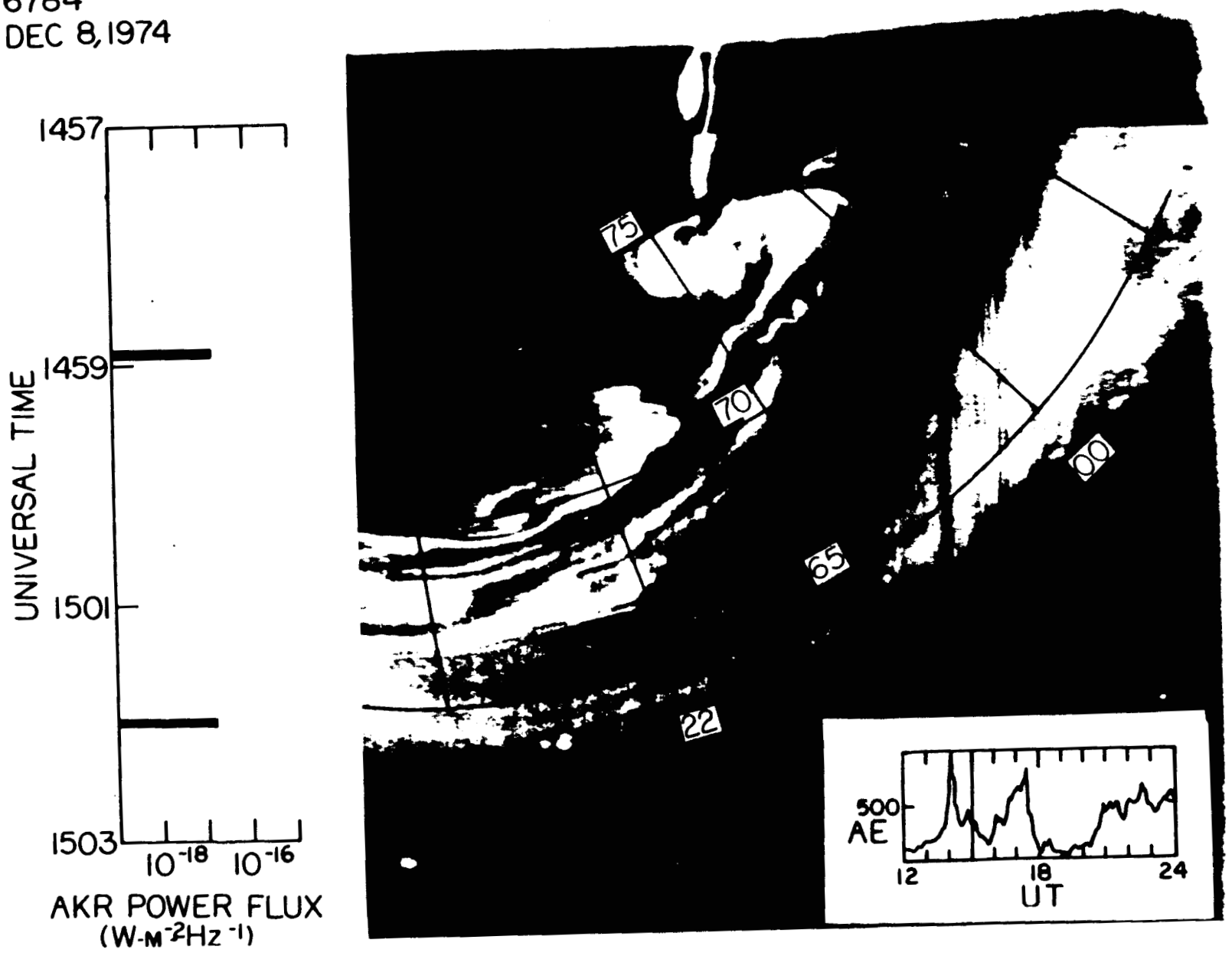

FIGURE 12

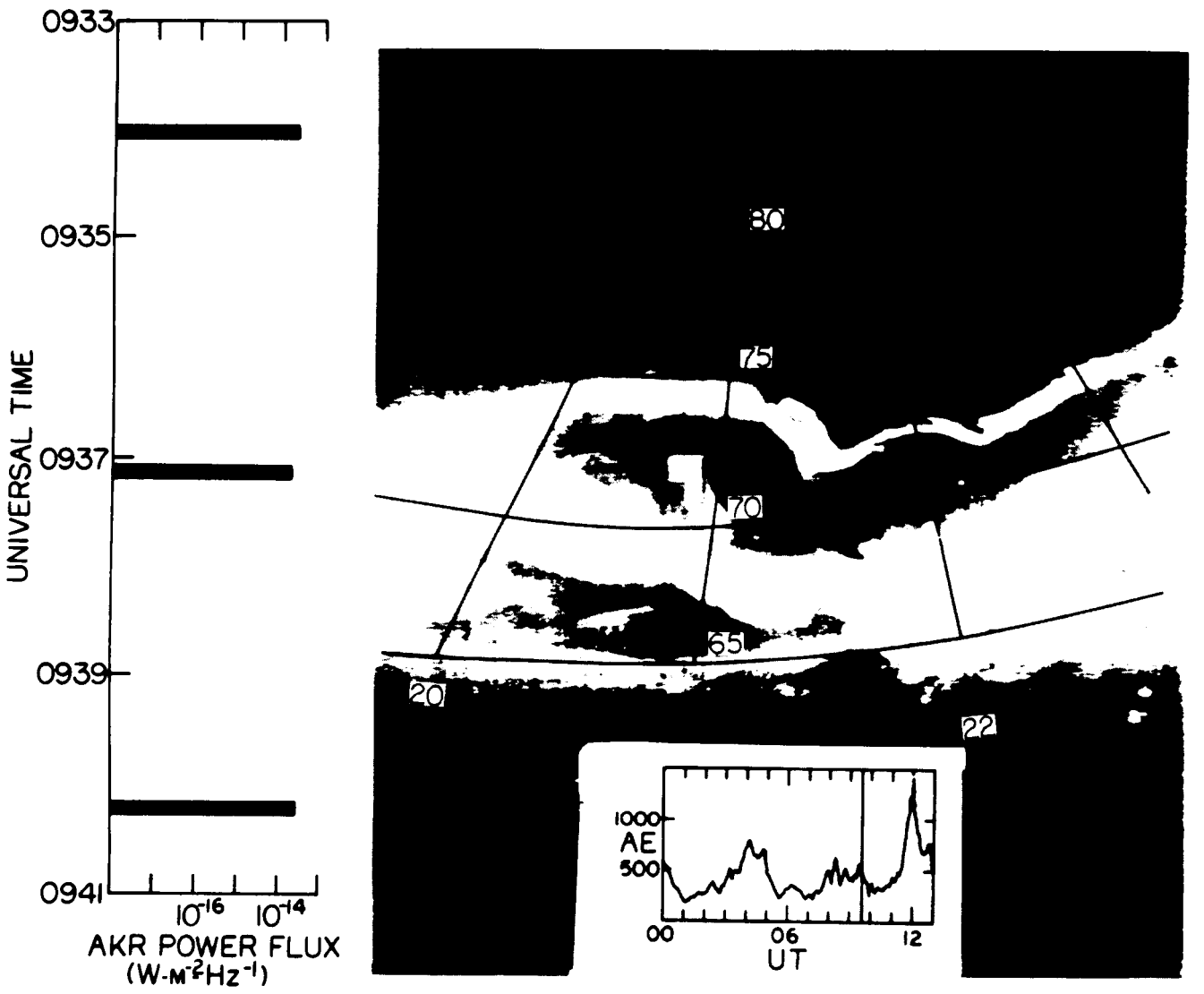

FIGURE 13

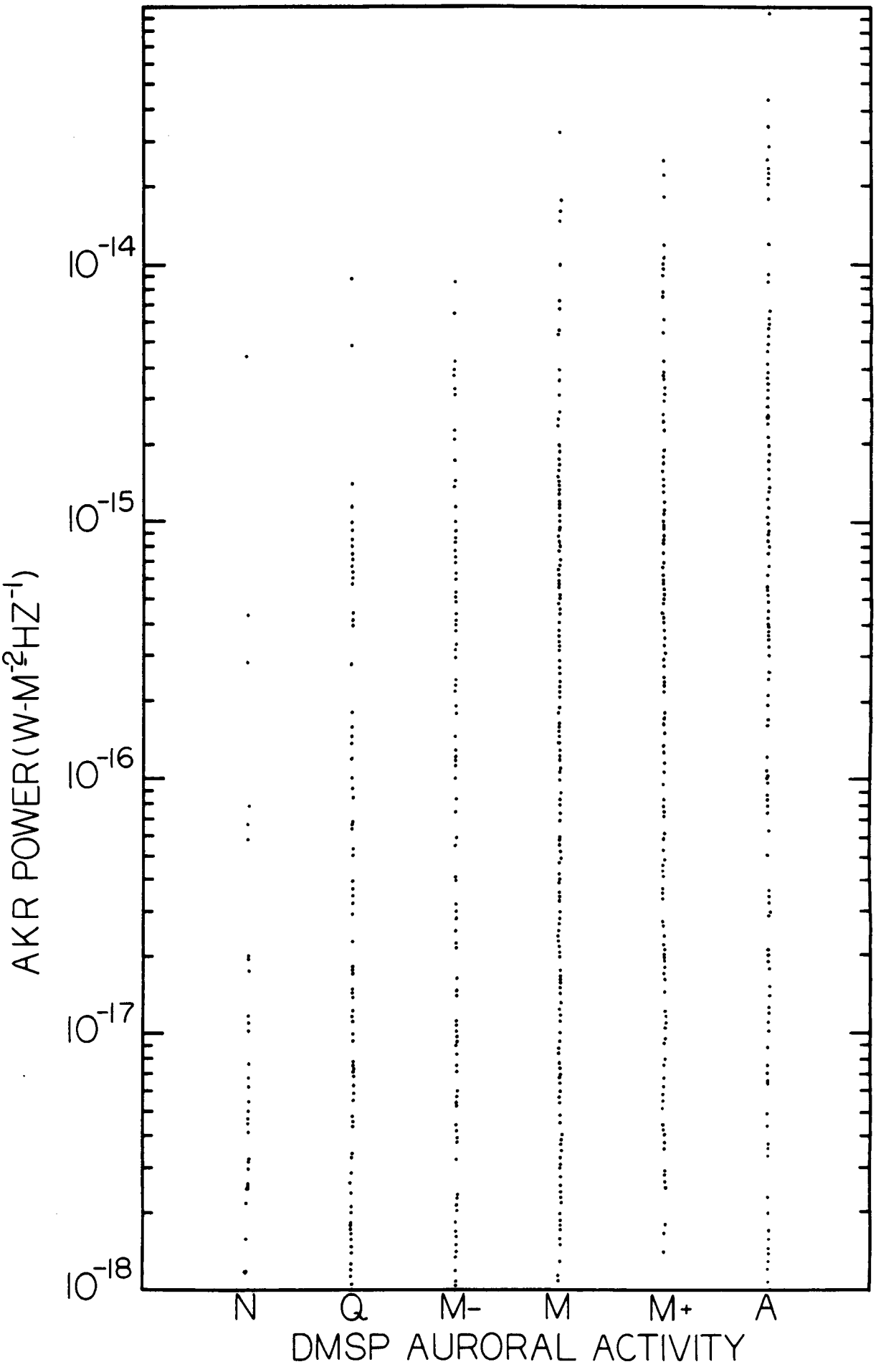
AKR POWER(W-M-2HZ-1)
10-14
10-15
10-16
10-17
10-18
N
Q
M-
M
M+
A
DMSP AURORAL ACTIVITY

FIGURE 14

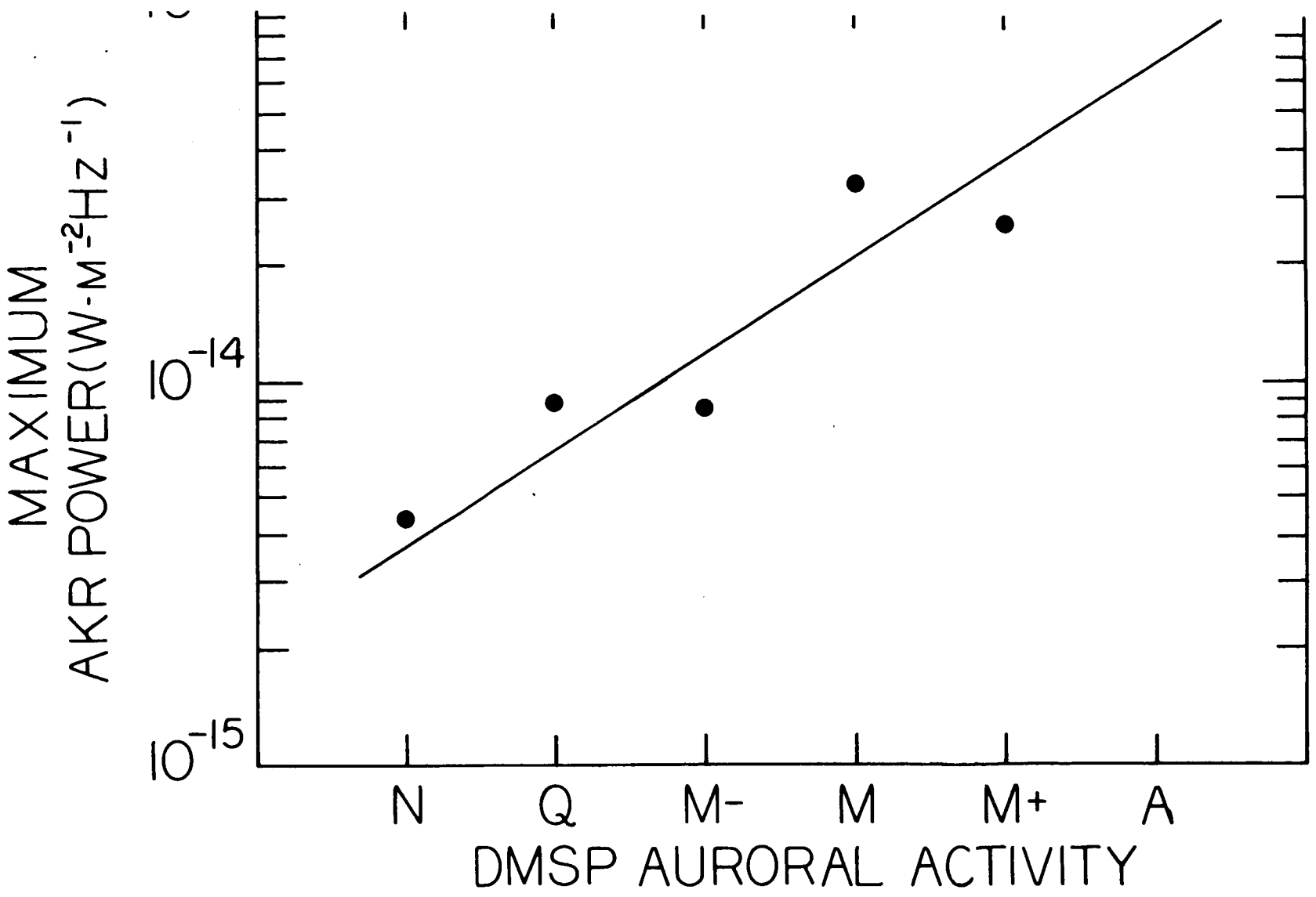
MAXIMUM
AKR POWER(W-M^{-2}HZ^{-1})
10^{-14}
10^{-15}
N
Q
M-
M
M+
A
DMSP AURORAL ACTIVITY

FIGURE 15

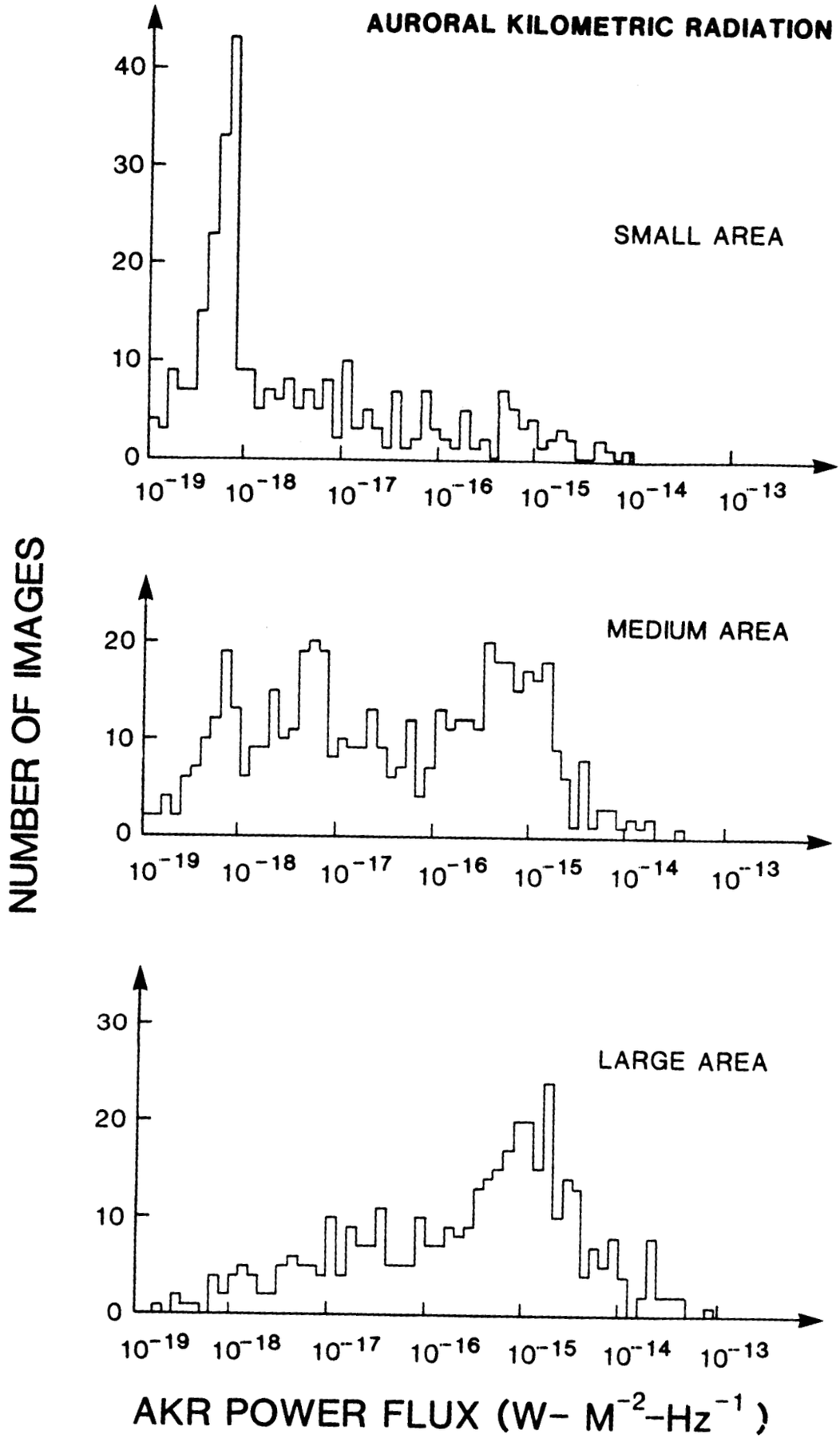
AURORAL KILOMETRIC RADIATION
SMALL AREA
MEDIUM AREA
LARGE AREA
NUMBER OF IMAGES
AKR POWER FLUX (W- M^{-2}-Hz^{-1})
40
30
20
10
0
10^{-19} 10^{-18} 10^{-17} 10^{-16} 10^{-15} 10^{-14} 10^{-13}

FIGURE 16